Supporting Information

Ultrasmall MoC Supported PtRu Clusters with Boosted HOR Activity and CO Tolerance via Metal-Support Interaction

Yaheng Gu,†[ab] Shaoqing Zhang,†[ab] Zihao Li,[ab] Dezheng Zhang,[ab] Jianzhi Liu,[ab] Mingda Zhao,[ab] Ce Han,[a] Xiue Jiang,*[abc] Ping Song,*[a] and Weilin Xu*[ab]

[a] Key Laboratory of Electroanalytical Chemistry, Changchun Institute of Applied Chemistry, Chinese Academy of Sciences, Changchun 130022, P.R. China.

[b] School of Applied Chemistry and Engineering, University of Science and Technology of China, USTC, Hefei 230026, China.

[c] Research Center for Analytical Science, College of Chemistry, Nankai University, Tianjin, 300071 China.

*Corresponding Author email: xiuejiang@nankai.edu.cn; songping@ciac.ac.cn; weilinxu@ciac.ac.cn;

Experimental section

Chemicals

Ruthenium chloride ($RuCl_3$), Chloroplatinic acid hexahydrate ($H_2PtCl_6 \cdot 6H_2O$), Potassium hydroxide (KOH) and Copper sulfate pentahydrate ($CuSO_4 \cdot 5H_2O$) were obtained from Beijing InnoChem Science & Technology Co., Ltd. Vulcan XC-72 was purchased from Carbot. Nafion solution (5 wt%) was purchased from Alfa Aesar. Sulfuric acid (98%, H_2SO_4) was purchased from Beijing Chemical Works. 20 wt% commercial PtC (Pt/C_{com}), Cyanuric acid ($C_3H_3N_3O_3$) and Ammonium molybdate tetrahydrate ($(NH_4)_6Mo_7O_{24} \cdot 4H_2O$) were purchased from Aldrich Chemical. 20 wt% commercial RuC (Ru/C_{com}) and 20 wt% commercial PtRuC ($PtRu/C_{com}$, Pt/Ru=1:1) were purchased from Premetek. Melamine ($C_3H_6N_6$) was purchased from Shanghai Macklin Biochemical Technology Co., Ltd. Ethanol (99.7%, C_2H_6O) was purchased from Xilong Scientific Co., Ltd. The water for the experiments (18.25 MΩ·cm) was obtained using a Millipore Ultrapure water system. All of the chemicals were firsthand utilized with no further treatment.

Synthesis of MoC

In a typical synthesis, 0.03 mol Melamine and 0.03 mol Cyanuric acid were dispersed in 120 mL water by ultrasonic dispersion for 30 min. Then, a 30 mL solution containing 1.86g $(NH_4)_6Mo_7O_{24} \cdot 4H_2O$ was slowly dropped into the above milky solution and kept the mixture for 12 h under continuous magnetic stirring at room temperature. The obtained precipitates were collected by centrifugation at 8500 rpm, washed three times with ethanol and water. After the precursor was dried in vacuum at 50℃ overnight, it was grinded into powder and annealed in a tube furnace under an Ar atmosphere at 700 °C for 3 h with a heating rate of 5 °C min^{-1}.

Synthesis of PGM/MoC and PGM/C

Briefly, 95 mg MoC or Vulcan XC-72 was dispersed in 80 mL water by ultrasonic dispersion for 30 min to form a uniform slurry, then a certain amount of $H_2PtCl_6 \cdot 6H_2O$ aqueous solution (9.8 mg_{Pt} mL^{-1}) and $RuCl_3$ aqueous solution (11.28 mg_{Ru} mL^{-1}) were added into the above solution. The homogeneous solution

was stirred for 6 h and then dried in a rotary evaporation at 50 ℃. Finally, the catalyst was obtained by grinded into powder and annealed under 5% H_2/Ar atmosphere at 500 °C for 3 h with a heating rate of 5 °C min^{-1}.

Material characterizations

X-ray powder diffraction (XRD) data were recorded on an X-ray diffractometer (D8 ADVANCE) with Cu Kα radiation at a scan rate of 2° min^{-1} in the 2θ range from 5° to 90° (λ=1.5413). The morphology and microstructure of as-prepared samples were characterized under a XL 30 ESEMFEG field emission scanning electron microscopy (SEM). High-resolution transmission electron microscopy (HRTEM), HADDF-STEM images and EDS elemental mapping were performed on a TECNAI G2 transmission electron microscope at an accelerating voltage of 200 kV. The surface electronic states and valence band spectroscopy (XPS) were measured with a Thermo Fisher Scientific ESCALAB 250Xi. The parameters of XPS testing are as follows: Total acquisition time: 1 min and 10.3 secs; Source Gun Type: Al K Alpha; Spot Size: 400 μm; Lens Mode: Standard; Analyzer Mode CAE: Pass Energy 30.0 eV; Energy Step Size: 0.100 eV; Number of Energy Steps: 281. XPS data were fitted by Avantage software, and the detailed fitting parameters are shown in Table S2-5 and Table S9-13. Specifically, XPS spectra were calibrated using the C 1s peak at 284.8 eV as a reference. All spectra were fitted after smart background subtraction using mixed Gaussian-Lorentzian line shapes. The chemical composition of materials was obtained from ICP-MS measurement (Thermo Fisher Scientific). Raman spectra were acquired using a LabRAM HR EVO confocal Raman spectrometer (HORIBA, Japan) equipped with a 633 nm laser. Each spectrum was accumulated over multiple scans to improve the signal-to-noise ratio. Nitrogen adsorption-desorption isotherms were measured at 77.35 K using an ASAP 2020 analyzer (Micromeritics, USA). The samples were degassed at 200 °C prior to measurement, and the specific surface area and pore structure were analyzed using the BET method based on the adsorption-desorption data.

CO temperature programmed desorption (CO-TPD)

CO-TPD tests were performed on Quantachrome Autosorb. He gas at a flow rate of 30 mL min^{-1} was used as carrying gas for CO TPD measurements. In a typical procedure, 50 mg sample was placed in a quartz

tube. He was injected into the tube for 15 min, and then the tube was heated to 250 ℃ at a rate of 10 ℃ min^{-1} and kept for 1 h under He atmosphere. The tube was then cooled down to 50 ℃. 10% CO/90% He was injected to the tube for 1 h and He flow was switched for 1 h to remove the weak physical adsorption CO on the surface. The thermal conductivity detector was switched on. TPD experiment was started when the baseline was stable. The tube was ramped up to 600 ℃ with a heating rate of 10 ℃ min^{-1} in He atmosphere.

In-situ ATR-SEIRAS Measurements

In-situ ATR-SEIRAS measurements were recorded using a Fourier transform infrared (FTIR) spectrometer (IFS 80v, Bruker, Ettlingen, Germany). A ZnSe prism was used as the attenuated total reflection crystal. The Au film deposition procedure was modified from the literature: the ZnSe was polished with 1 μm aluminum powder and then sequentially sonicated in ethanol, acetone, and ultrapure water to obtain a clean, powder-free surface. After drying the surface under the N_2 flow, the crystal was heated to 40 °C, one milliliter of 24 mM $HAuCl_4$ solution (also pre-heated to 40 °C) was added to the crystal surface for the chemical deposition of an Au film. After approximately 75 seconds, the reaction was stopped by dilution with ultrapure water, and the Au-coated ZnSe was cleaned with ultrapure water and dried under the N_2 flow. Successful Au deposition was confirmed by a surface resistance in the range of 15-30 Ω. Then 10 μL ink of catalyst (5 mg_{cat} mL^{-1}) was dropped onto the Au-coated ZnSe to form a uniform thin film. The crystal was fixed to a homemade spectra-electrochemical cell, a Kretschmann-ATR setup was adjusted to an incident angle of 60° to collect the infrared beam from the interferometer. The electrolyte was 0.1 M KOH. Before the measurements, a cyclic voltammetry (CV) scan from -0.1 V to 0.2 V was applied to the electrode under N_2 purging to activate the catalyst surface. The background spectrum was collected after holding the electrode potential at 0.2 V versus RHE for 5 min. Afterwards, chronoamperometry at different potential was conducted for each sample, and the corresponding spectral data were recorded simultaneously. According to the experimental requirements, the spectra were averaged over 256 scans, collected at a resolution of 4 cm^{-1}, with a scanner velocity of 80 kHz, and detected using a liquid-nitrogen-cooled mercury cadmium telluride (MCT) detector.

Electrochemical measurements

All the electrochemical performances were carried out in a regular three-electrode system by the CHI 750E electrochemical workstation (Chenhua, Shanghai). A graphite rod and an Ag/AgCl electrode were used as the counter and reference electrode. To prepare the catalyst ink, 5 mg catalysts powder were redispersed in a mixture of 950 μL of isopropanol and 50 μL of 5 wt% Nafion, then ultrasonicated for 30 min to form a homogenous ink. A certain amount of the catalyst ink was taken out and coated on a glassy carbon (GCE, diameter: 5 mm, area: 0.196 cm^2) on Rotating Ring-Disk Electrode (DC DSR ROTATOR, PHYCHEM), which was used as a working electrode after dried at room temperature. To ensure a fair and quantitative comparison, all electrochemical measurements were carried out under the same noble-metal loadings on the working electrode. It should be noted that the PGM loading was maintained at 5 μg cm^{-2} for intrinsic activity evaluation the LSV measurements on RDE to achieve higher mass activity and exchange current density, whereas the loading of 10 μg cm^{-2} was employed for the other electrochemical characterizations. In this work, all potentials mentioned were calibrated to the reversible hydrogen electrode (RHE):

$$E(RHE) = E(Ag/AgCl) + 0.059 * pH + 0.199 \quad (1)$$

HOR activity test: For the HOR test, the linear sweep voltammograms (LSV) polarization curves were performed in H_2-saturated 0.1 M KOH solution at a scan rate of 5 mV s^{-1} and rotation speed of 1600 rpm with 90% IR compensation.

CO stripping experiment: CO stripping test was performed in 0.1 M KOH solution. First, the electrode was held at a certain potential for 10 min in CO-saturated 0.1 M KOH solution. Then, the electrode was transferred rapidly to the N_2-saturated 0.1 M KOH solution, and CV curves were collected in the potential range from 0 to 1.25 V (vs. RHE) at a scan rate of 20 mV s^{-1}. The obtained first forward scan was considered as the stripping of a monolayer of CO.

H_{upd} experiment: The hydrogen adsorption behavior was evaluated by the desorption of the underpotential deposited hydrogen (H_{upd}), where CV was performed in the potential range from 0.02 to 0.6 V (vs. RHE) at a scan rate of 20 mV s^{-1} in N_2-saturated 0.1 M KOH solution.

HOR stability evaluation: The accelerated durability test was performed between 0 and 0.35 V (vs. RHE) for 1000 and 1500 cycles at a scanning rate of 150 mV s^{-1}. The chronoamperometry tests were carried out in H_2-saturated or H_2/1000 ppm CO-saturated 0.1 M KOH solution at a rotation speed of 1600 rpm.

The catalyst-modified gas diffusion electrode (GDE) was prepared by using carbon paper as electrode substrate. A 1×1 cm^2 catalyst-modified active area was formed by pipetting the catalyst ink onto the carbon paper and drying it at 40 ºC. The catalyst loading on GDE was 0.1 $mg_{PGM}cm^{-2}$. Chronoamperometry tests (i-t) were carried out under a constant potential of 0.1 V in H_2-saturated 0.1M KOH.

J_k and J_0 calculation: The HOR polarization curves under different rotation speeds (2500, 1600, 900 and 400 rpm) were measured at 5 mV s^{-1}. The kinetic current density (j_k) can be obtained from the Koutecky-Levich equation:

$$\frac{1}{j} = \frac{1}{j_k} + \frac{1}{j_d} \quad (2)$$

where j is measured current and j_d is diffusion-limited current, which can be collected by the Levich equation:

$$j_d = 0.62nFD^{3/2}v^{-1/6}C_0\omega^{1/2} = BC_0\omega^{1/2} \quad (3)$$

in which n is the number of electrons involved in the HOR, F is the Faraday constant, D is the diffusion coefficient of the reactant, v is the viscosity coefficient of electrolyte, C_0 is the solubility of H_2 in the electrolyte, ω is the rotating speed, and B is the Levich constant.

The exchange current density (j_0) was deduced from Butler-Volmer equation:

$$j_k = j_0(e^{\frac{\alpha F\eta}{RT}} - e^{\frac{(1-\alpha)F\eta}{RT}}) \quad (4)$$

where η is the overpotential, F is the Faraday constant, R is the universal gas constant, T is the Kelvin temperature, and α is the transfer coefficients. In micro-polarization regions, this equation can be simplified as:

$$j_0 = \frac{j}{\eta}\frac{RT}{F} \quad (5)$$

ECSA measurement: To maintain methodological consistency and ensure a fair and quantitative comparison of electrochemical active surface area (ECSA) and intrinsic catalytic activity across all catalysts investigated, the Cu_{upd} method was uniformly adopted instead of CO stripping. Cyclic voltammetry was conducted in 0.5 M H_2SO_4 solution first to obtain the background. Then the electrode was quickly moved to a solution of 0.5 M H_2SO_4 containing 5 mM $CuSO_4$ in order to deposit Cu at 0.24 V (vs. RHE) for 100 s. At last, Cu_{upd} stripping voltammetry was performed in 0.5 M H_2SO_4 solution at the scan rate of 20 mV s^{-1}. The two curves were compared to calculate the ECSA of catalysts using Equations (6) and (7).

$$Q_{Cuupd}(C) = \frac{\int idE(mAV)}{v(mV/s)} \quad (6)$$

$$ECSA(\frac{m^2}{g}) = [\frac{Q_{Cuupd}(C)}{\frac{C}{420(\mu\frac{C}{cm^2})m_{PGM}(mg)}}]10^5 \quad (7)$$

where ν is the scan rate, i is the current and m_{PGM} is the mass of PGM on the electrode.

The Nernst diffusion limit is obtained from equation (8):

$$\eta_{diffision} = -\frac{RT}{2F}\ln(1 - \frac{i_d}{i_{lim}}) \quad (8)$$

where $\eta_{diffusion}$ is the diffusion-controlled overpotential and i_d is the H_2 diffusion-limited current density.

Computational details and theoretical models

All the computations were performed by using the Vienna ab initio Simulation Package (VASP)[1]. The electronic exchange and correlation effects were described by Perdew–Burke–Ernzerhof (PBE) formalism within a generalized gradient approximation (GGA)[2]. A kinetic cut-off energy of 500 eV was employed for the plane-wave basis and a Gaussian electron smearing of 0.05 eV was used. The convergence criteria for the energy and forces were 10^{-5} eV/atom and 0.001 eV $Å^{-1}$ respectively, which were chosen according to the previous literatures to ensure the accuracy[3]. Based on the description of structure and size for the catalysts, metal clusters with 13 atoms were conducted loading on MoC and graphene surface, respectively. Herein, the clusters model for alloy PtRu was built based on the Pt/Ru ratio of 1/2 from ICP results, and

the optimized structure for MoC was the exposure of Mo element rather than O exposure, consistent with the result from XPS without M-O bond and previous work.

The adsorption energies of hydrogen and hydroxyl species on different catalyst surface were calculated according to the following equations:

$$E_{ad-*H} = E_{cat-*H} - E_{cat} - E_{*H} \quad (9)$$

$$E_{ad-*OH} = E_{cat-*OH} - E_{cat} - E_{*OH} \quad (10)$$

$$E_{ad-*CO} = E_{cat-*CO} - E_{cat} - E_{*CO} \quad (11)$$

where $E_{\text{cat-*H}}$ and $E_{\text{cat-*OH}}$ represent the electronic energy of catalyst adsorbed hydrogen and hydroxyl species, respectively. Moreover, E_{cat}, E_{ad-*H}, E_{ad-*OH} and E_{ad-*CO} stand for the energies of the pure surface of catalyst, the isolated hydrogen atoms and the isolated hydroxyl species, respectively. A more negative E_{ad} indicates a larger binding energy.

The free energy change was acquired by:

$$\Delta G = E + E_{ZPE} - T\Delta S \quad (12)$$

where E is electronic energy, E_{ZPE} is the correction of zero-point energy (ZPE), ΔS is the entropy (S) variation, and T is the temperature (T = 298.15 K).

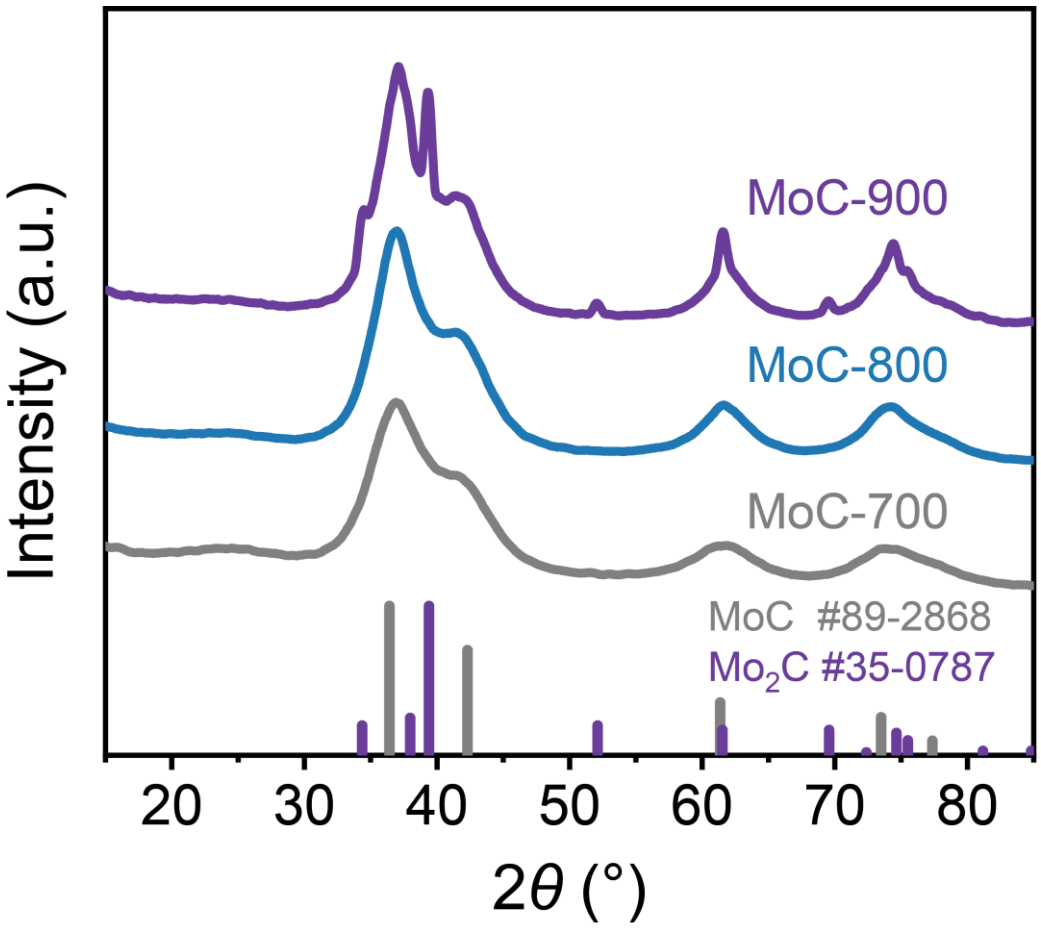

Figure S1. XRD patterns of MoC at different synthesis temperatures.

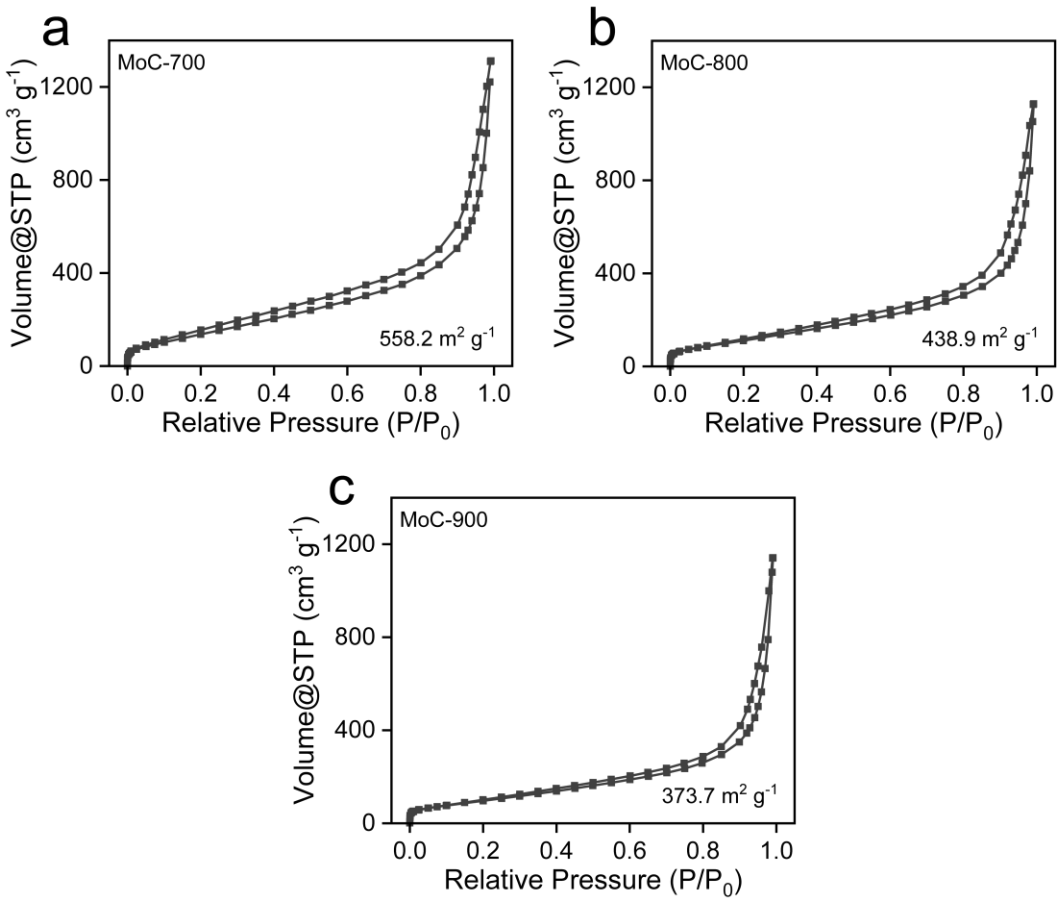

Figure S2. The N_2 adsorption-desorption isotherms of (a) MoC-700; (b) MoC-800; (c) MoC-900.

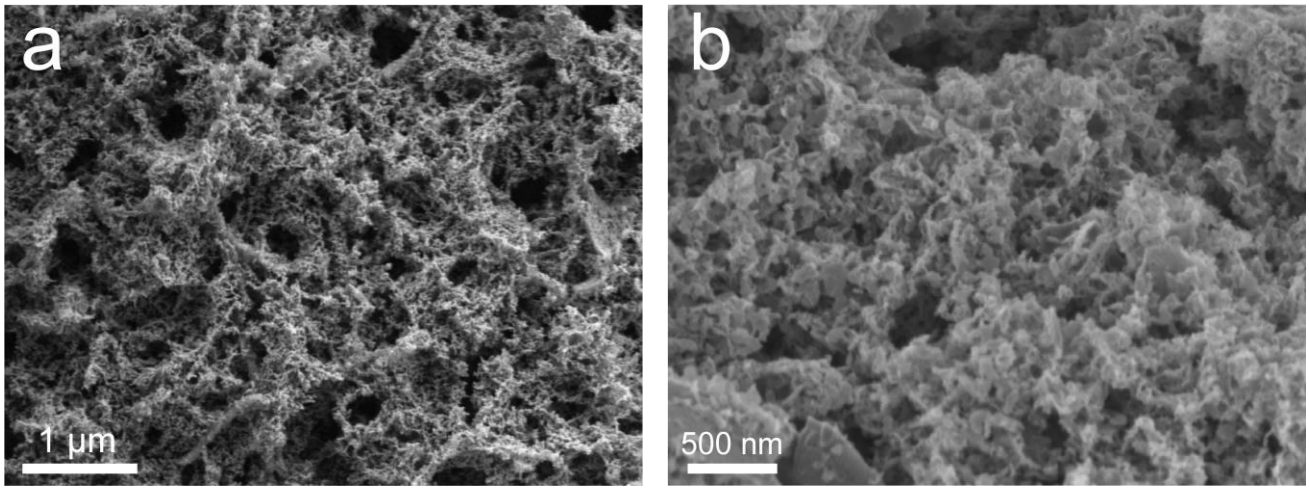

Figure S3. (a-b) SEM images with different magnifications of MoC-700.

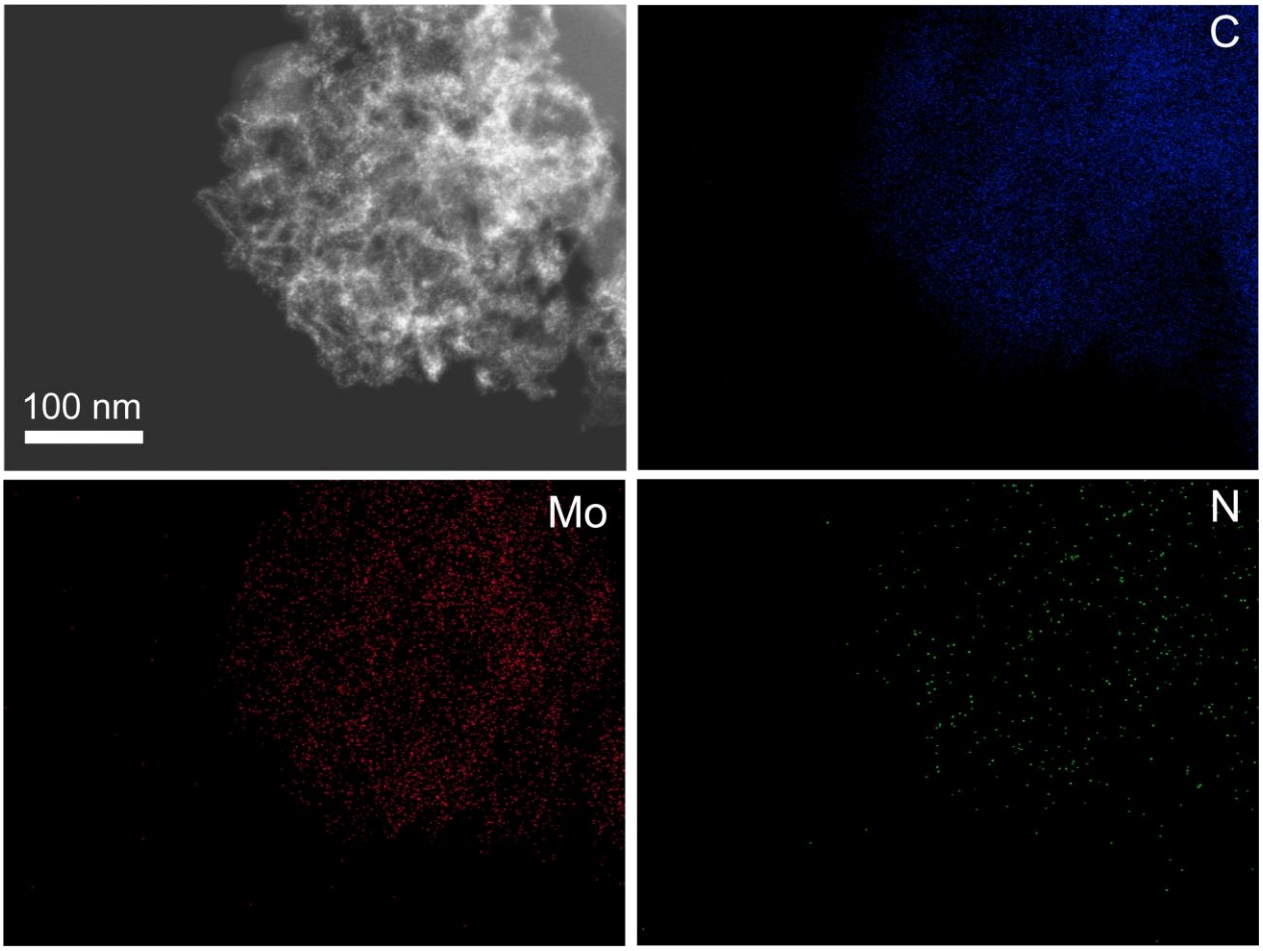

Figure S4. HAADF-STEM image and the corresponding EDS mapping images of MoC-700. The different colors depict the following: blue: C; red: Mo; green: N.

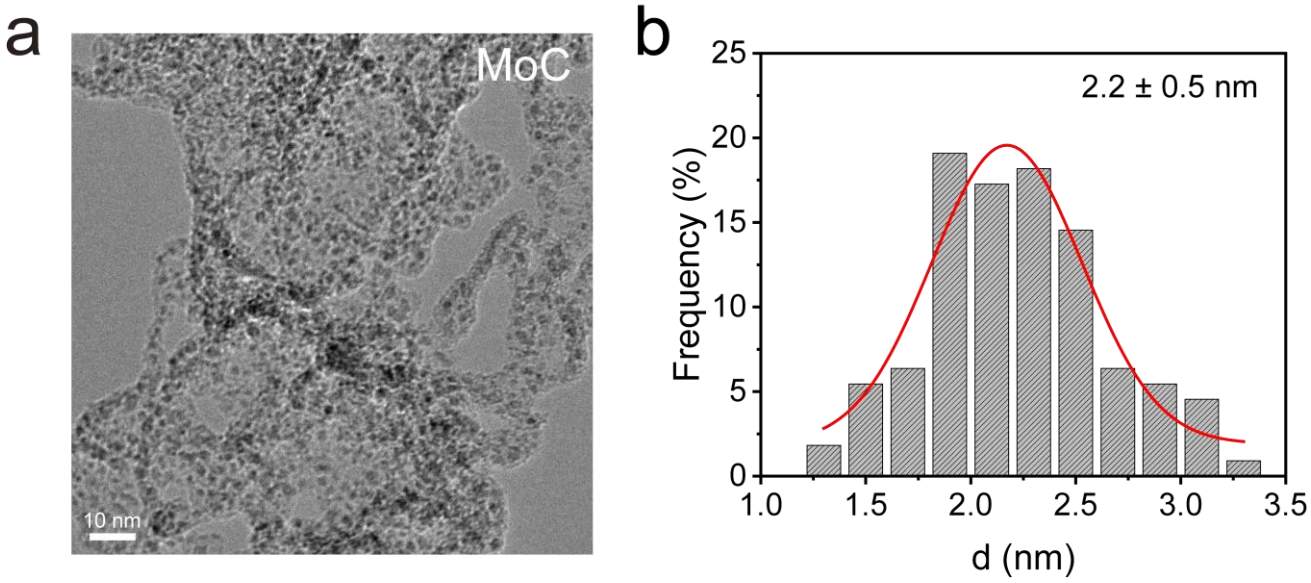

Figure S5. (a) TEM image and (b) size distribution of MoC-700.

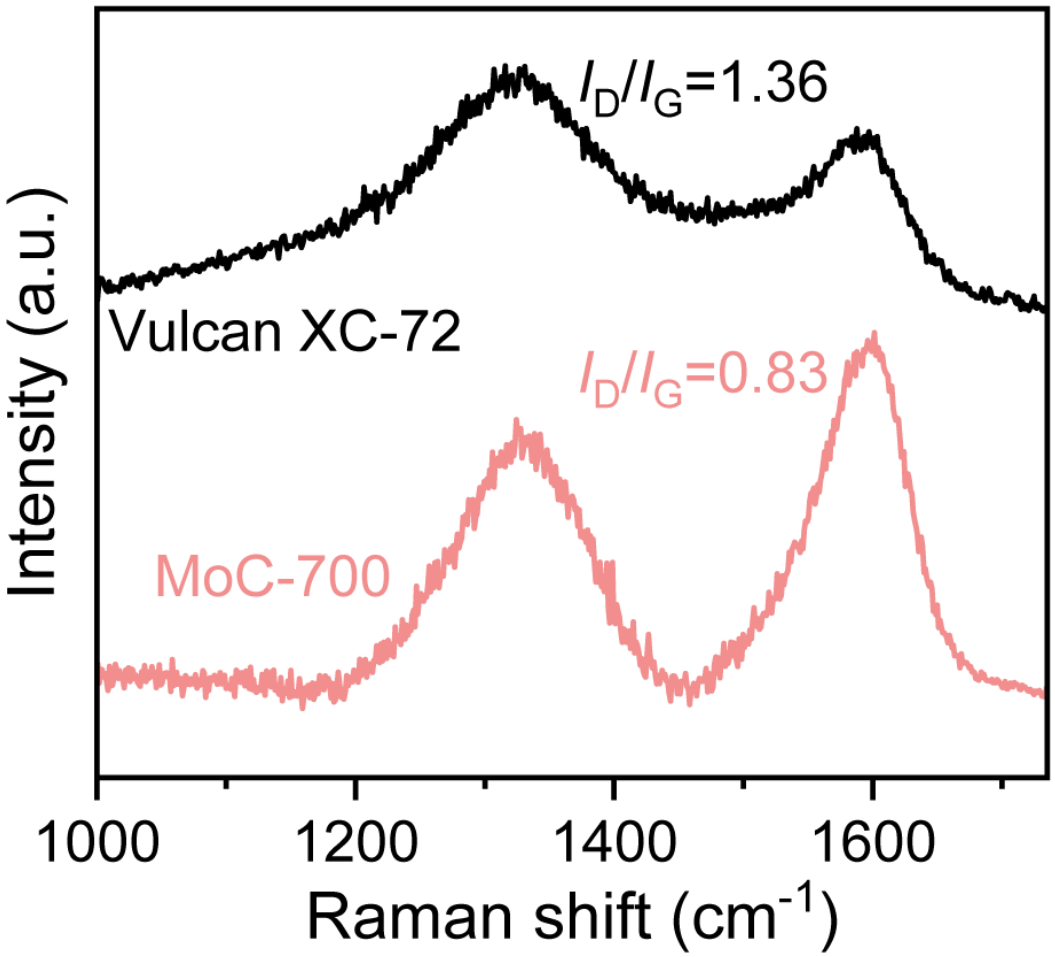

Figure S6. Raman spectra of Vulcan XC-72 and MoC-700.

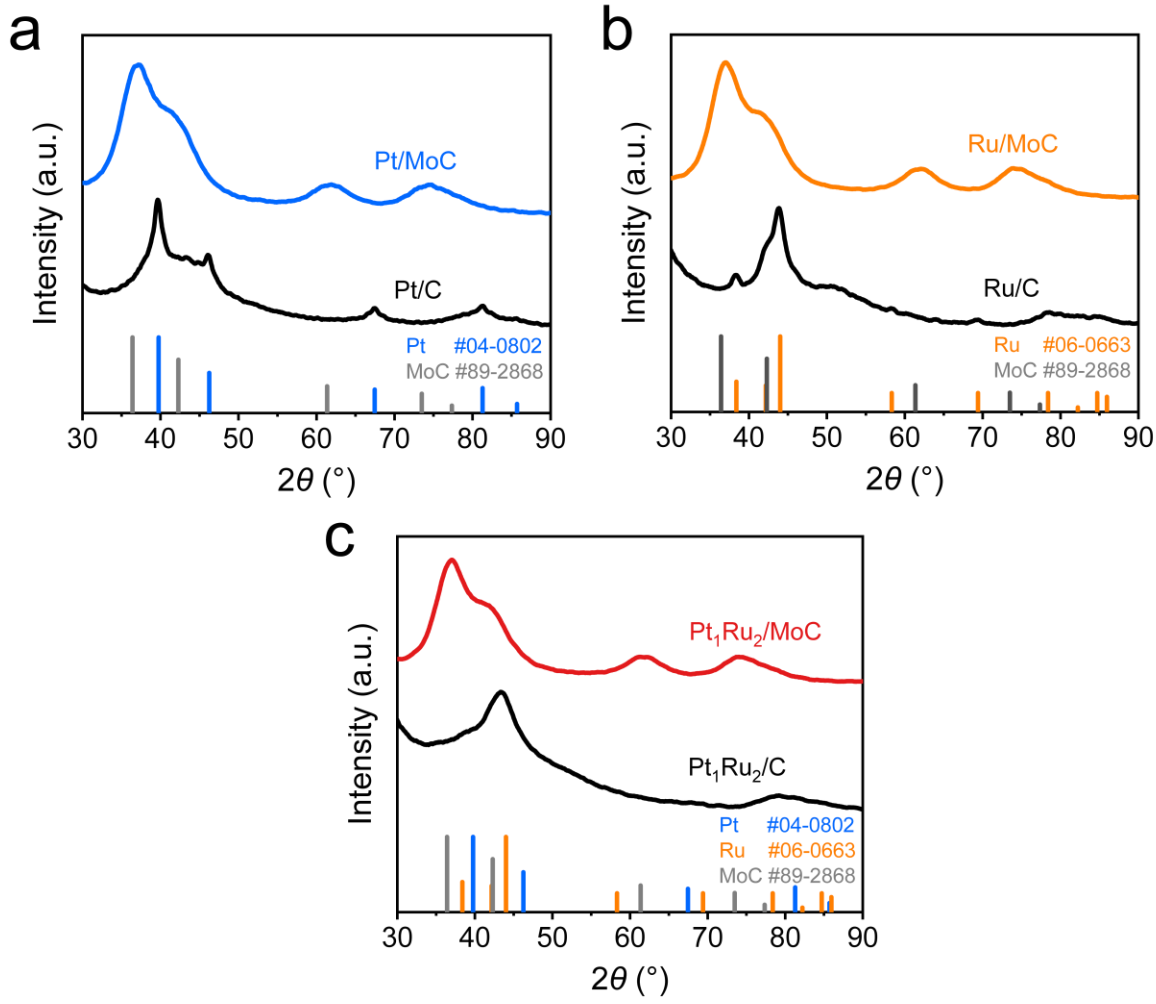

Figure S7. (a) XRD patterns of Pt/MoC and Pt/C; (b) XRD patterns of Ru/MoC and Ru/C; (c) XRD patterns of Pt_1Ru_2/MoC and Pt_1Ru_2/C.

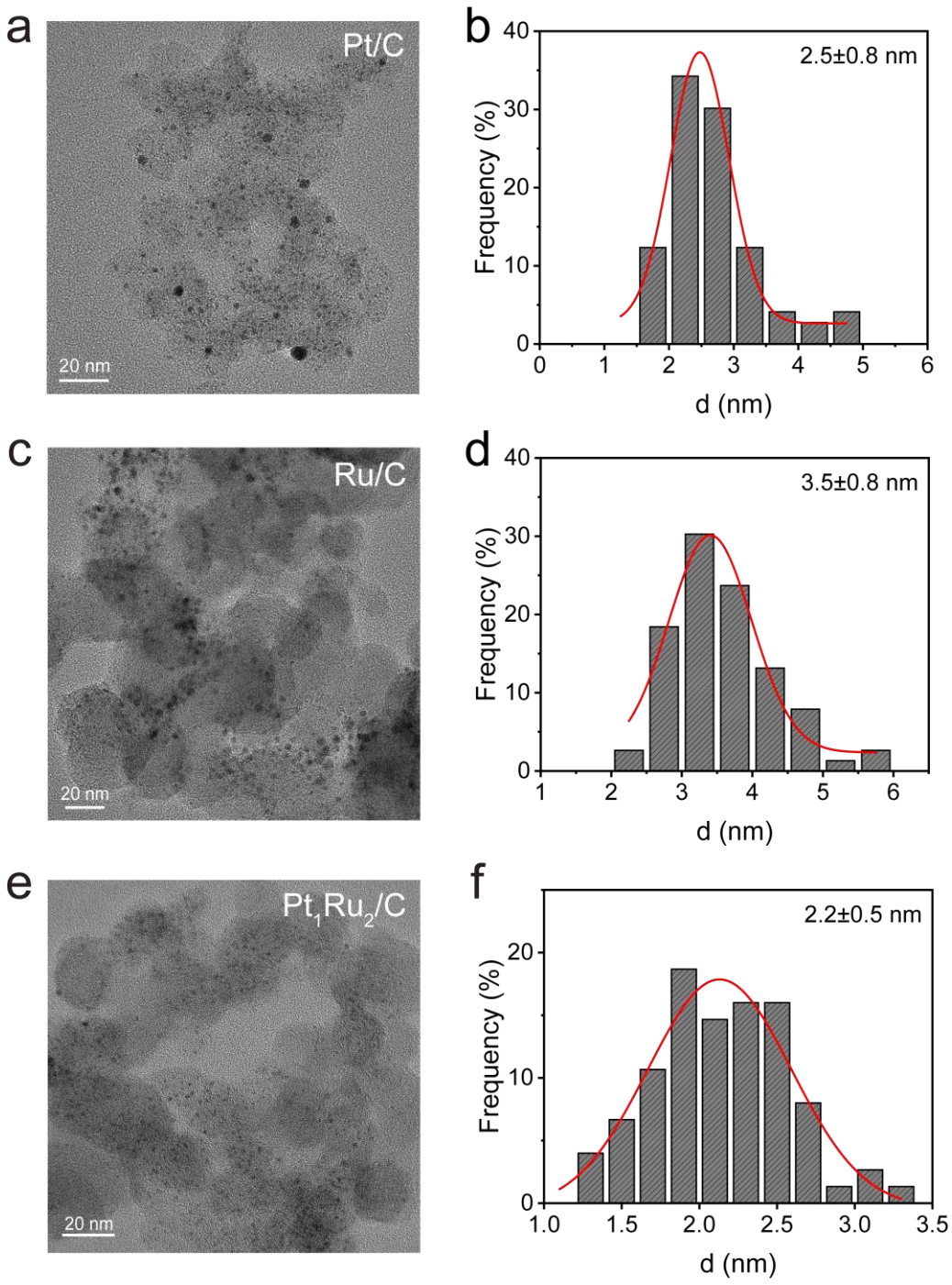

Figure S8. (a) TEM image and (b) size distribution of Pt/C; (c) TEM image and (d) size distribution of Ru/C; (e) TEM image and (f) size distribution of Pt_1Ru_2/C.

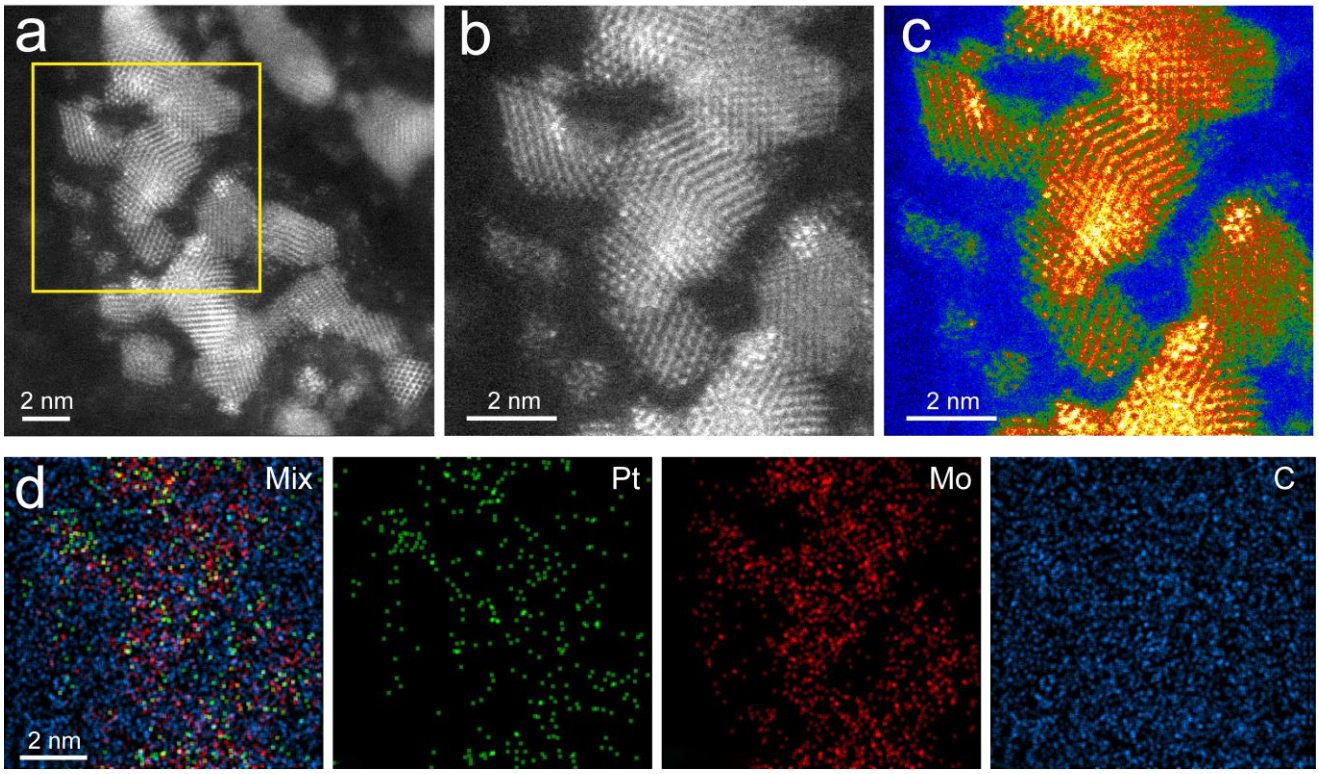

Figure S9. (a) AC-HAADF-STEM and (b) Enlarged AC-HAADF-STEM image of Pt/MoC. (c) Enlarged AC-HAADF-STEM image of Pt/MoC in grayscale mode, color model: Temperature. (d) Enlarged STEM EDS elemental mapping images of Pt/MoC.

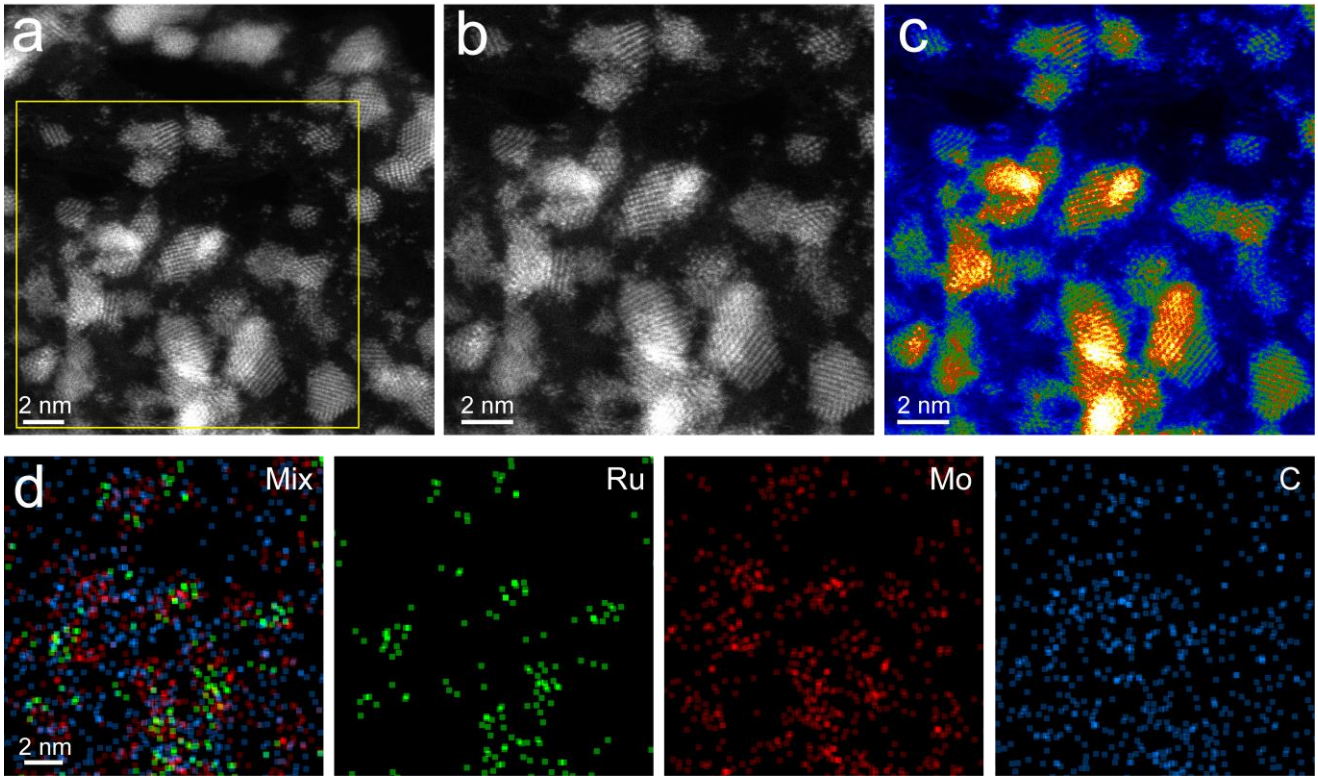

Figure S10. (a) AC-HAADF-STEM and (b) Enlarged AC-HAADF-STEM image of Ru/MoC. (c) Enlarged AC-HAADF-STEM image of Ru/MoC in grayscale mode, color model: Temperature. (d) Enlarged STEM EDS elemental mapping images of Ru/MoC.

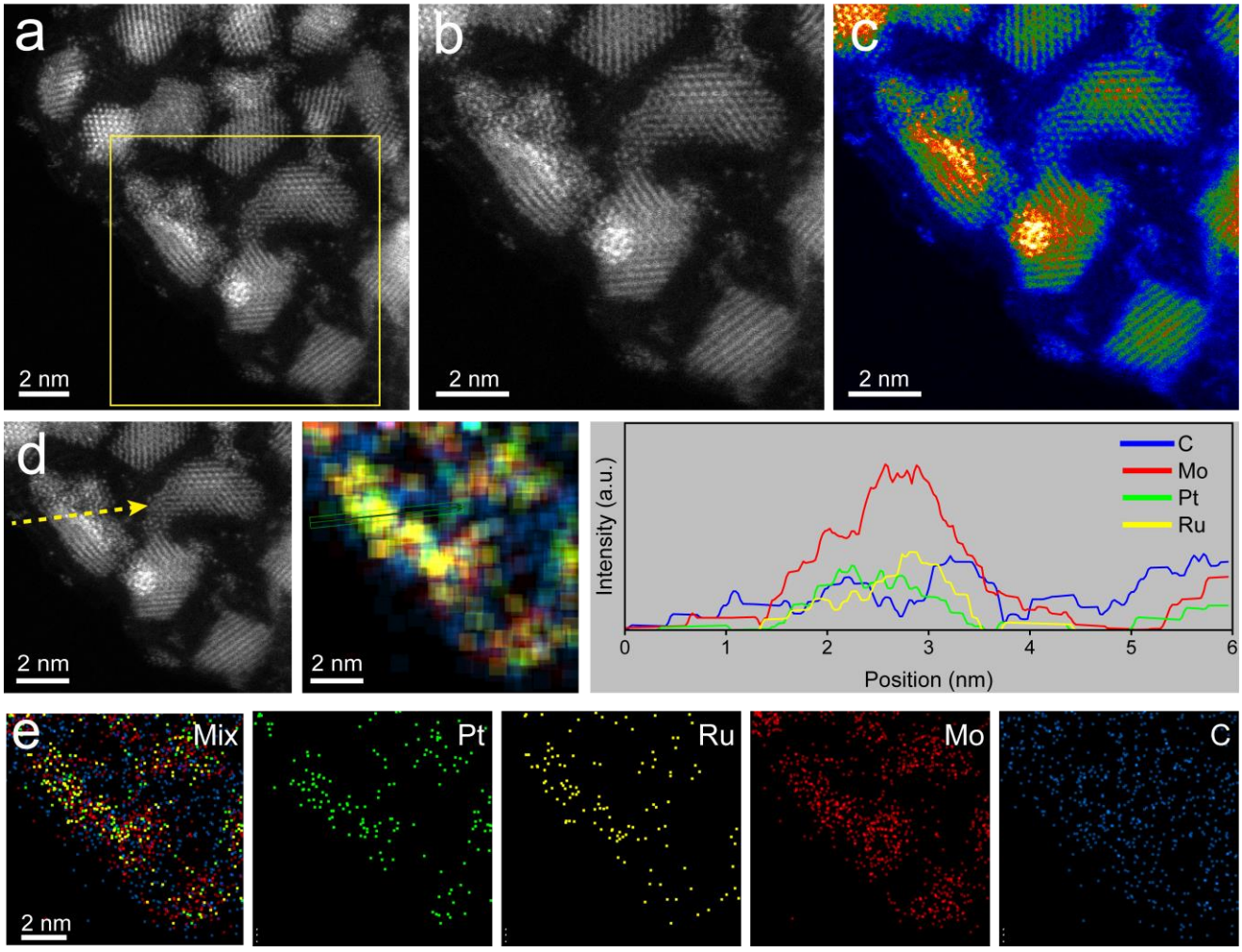

Figure S11. (a) AC-HAADF-STEM and (b) Enlarged AC-HAADF-STEM image of Pt_1Ru_2/MoC. (c) Enlarged AC-HAADF-STEM image of Pt_1Ru_2/MoC in grayscale mode, color model: Temperature. (d) EDS Line Scan images and results of Pt_1Ru_2/MoC in another region. (e) Enlarged STEM EDS elemental mapping images of Pt_1Ru_2/MoC.

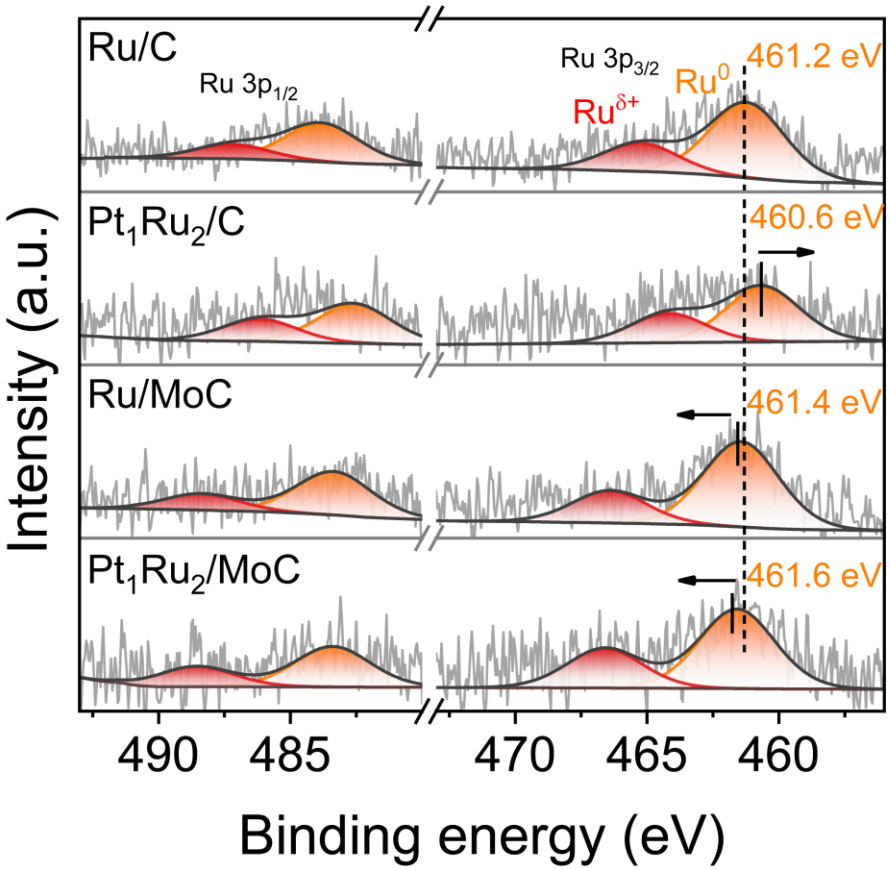

Figure S12. Ru 3p XPS spectra in Ru/C, Pt_1Ru_2/C, Ru/MoC and Pt_1Ru_2/MoC, respectively.

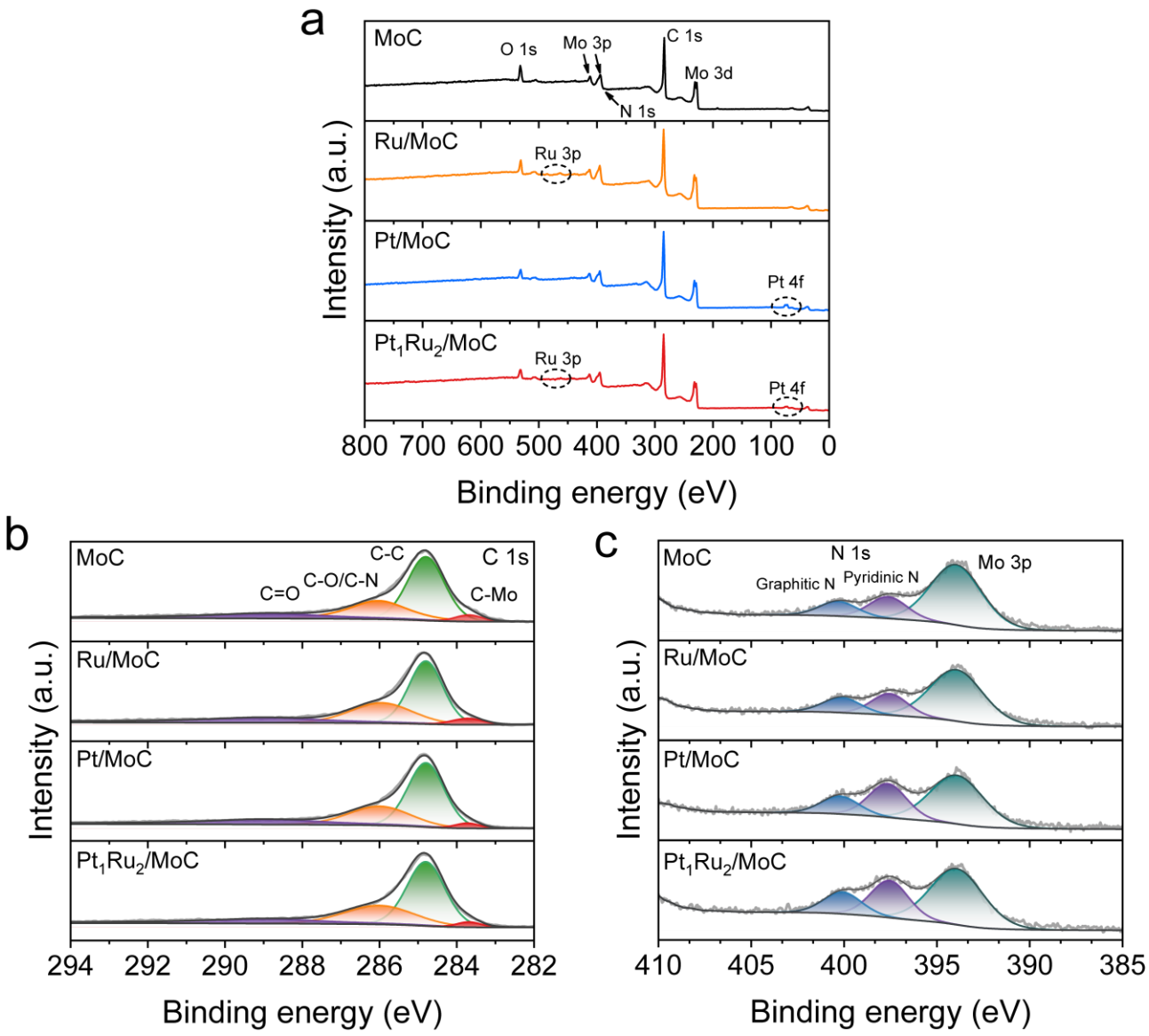

Figure S13. (a) XPS survey spectra of MoC, Ru/MoC, Pt/MoC and Pt_1Ru_2/MoC. The high-resolution XPS spectra of (b) C 1s and (c) N 1s for prepared samples.

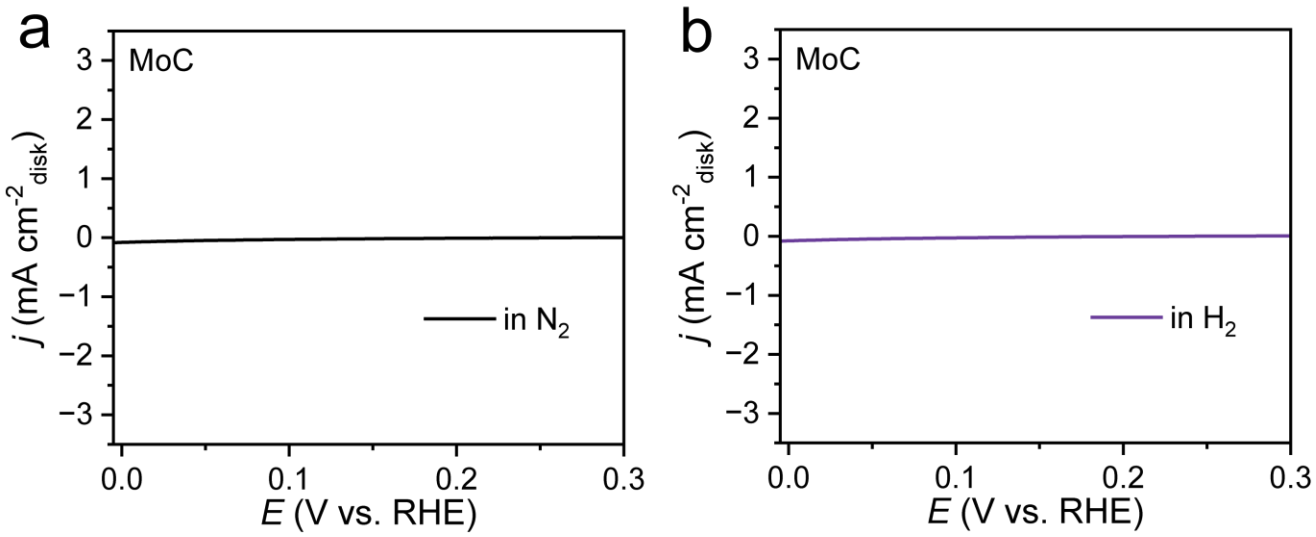

Figure S14. (a) HOR polarization curve of MoC in N_2-saturated 0.1 M KOH solution. (b) HOR polarization curve of MoC in H_2-saturated 0.1 M KOH solution.

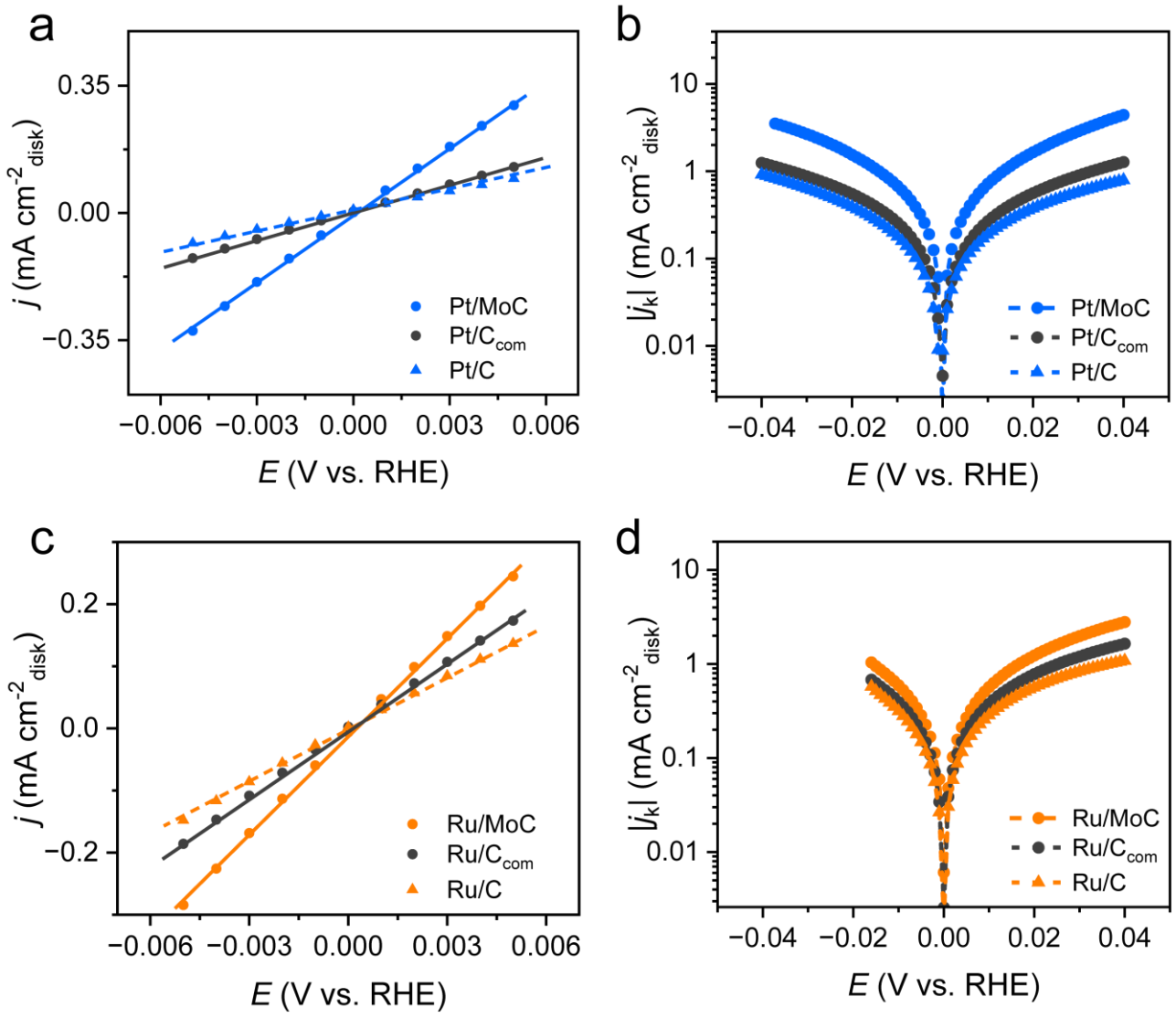

Figure S15. (a, c) Linear fitting curves at micropolarization region of different catalysts. (b, d) The HOR Tafel plots of kinetic current density (j_k).

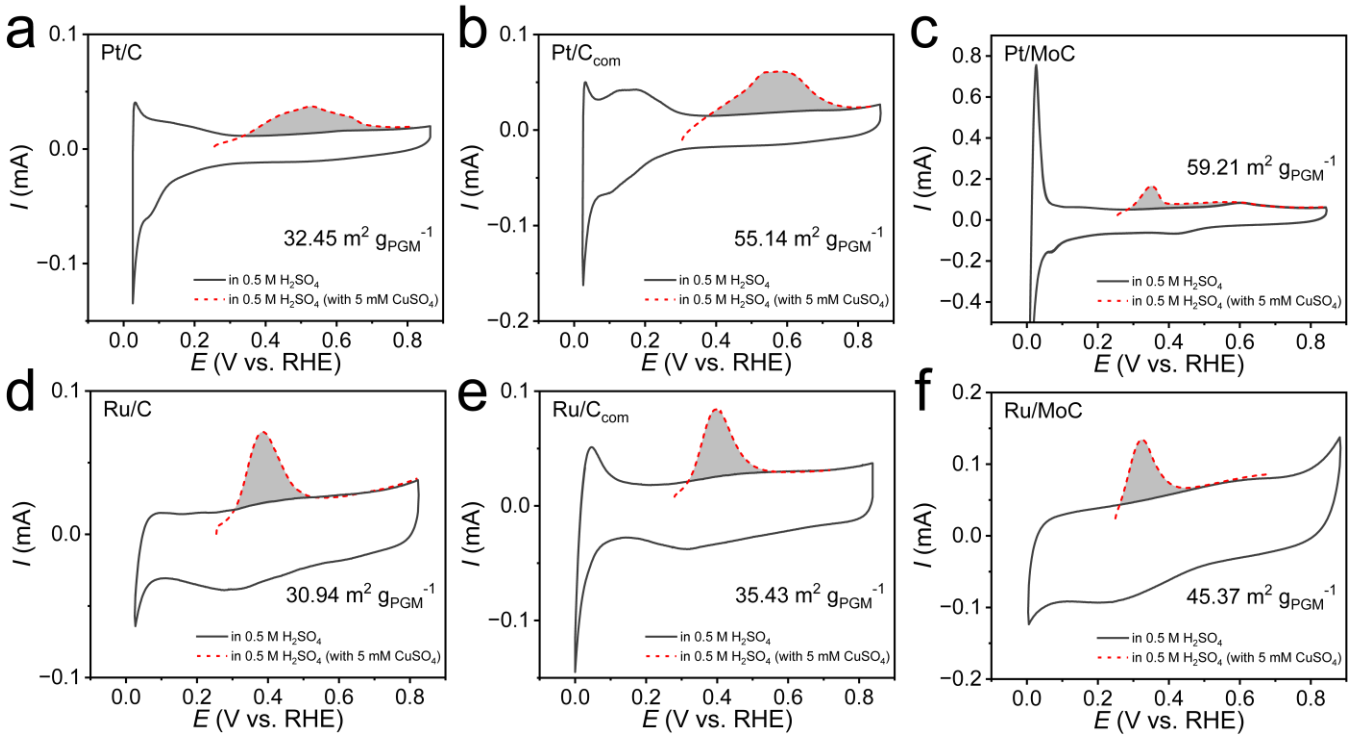

Figure S16. The Cu stripping curves of (a) Pt/C; (b) Pt/C_{com}; (c) Pt/MoC; (d) Ru/C; (e) Ru/C_{com} and (f) Ru/MoC.

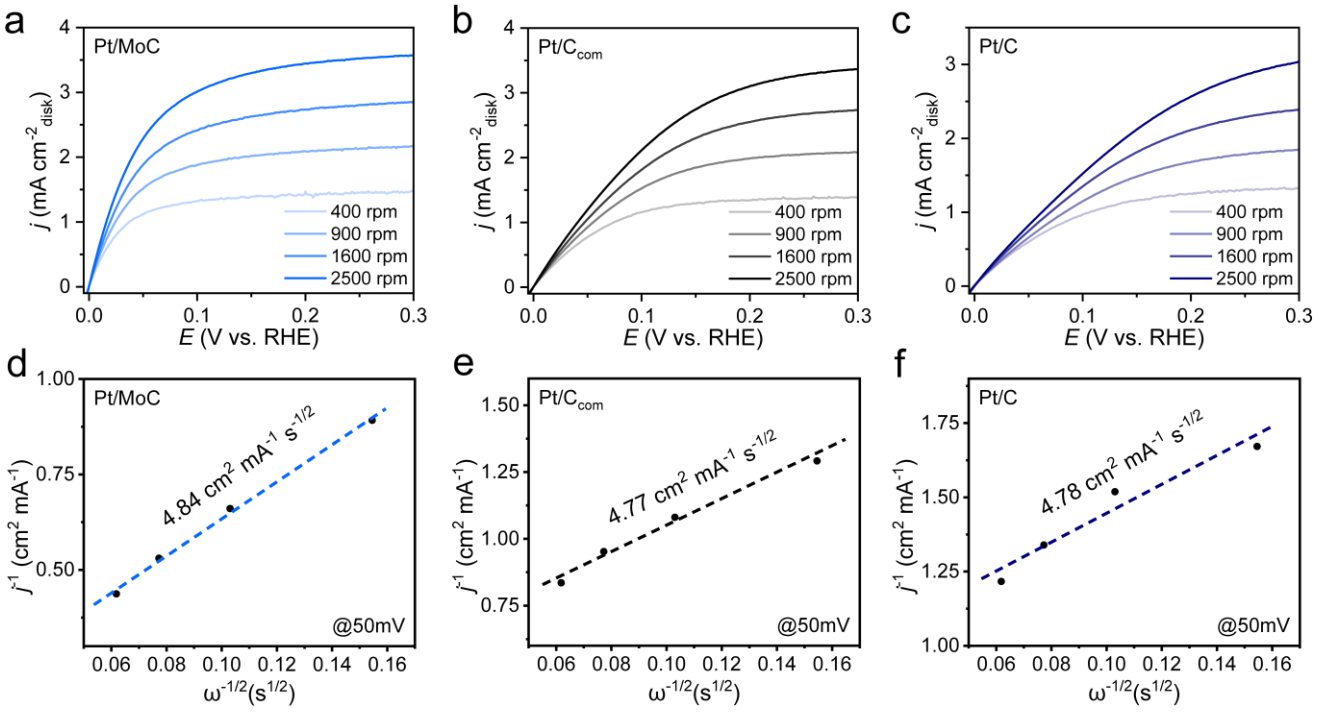

Figure S17. HOR polarization curves in H_2-saturated 0.1 M KOH at the rotating speeds varied from 400 to 2500 rpm of (a) Pt/MoC, (b) Pt/C_{com} and (c) Pt/C. Koutecky-Levich plot at an overpotential of 50 mV of (d) Pt/MoC, (e) Pt/C_{com} and (f) Pt/C.

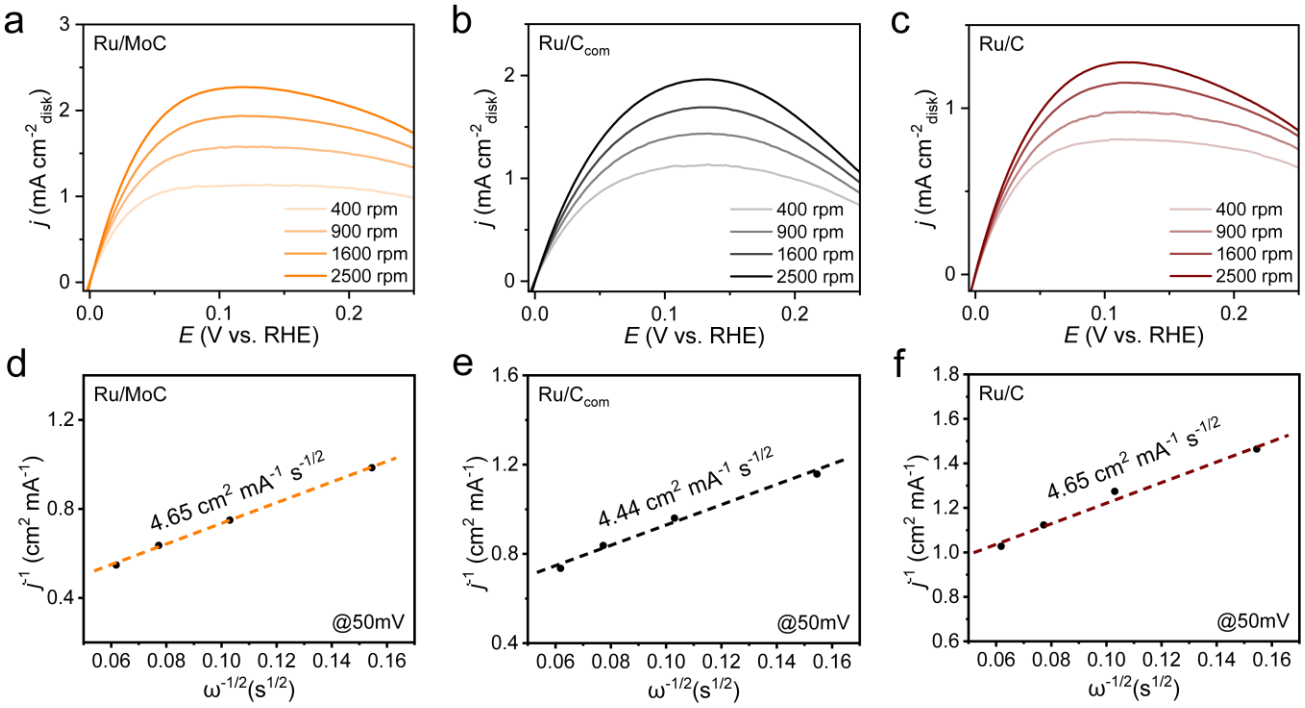

Figure S18. HOR polarization curves in H_2-saturated 0.1 M KOH at the rotating speeds varied from 400 to 2500 rpm of (a) Ru/MoC, (b) Ru/C_{com} and (c) Ru/C. Koutecky-Levich plot at an overpotential of 50 mV of (d) Ru/MoC, (e) Ru/C_{com} and (f) Ru/C.

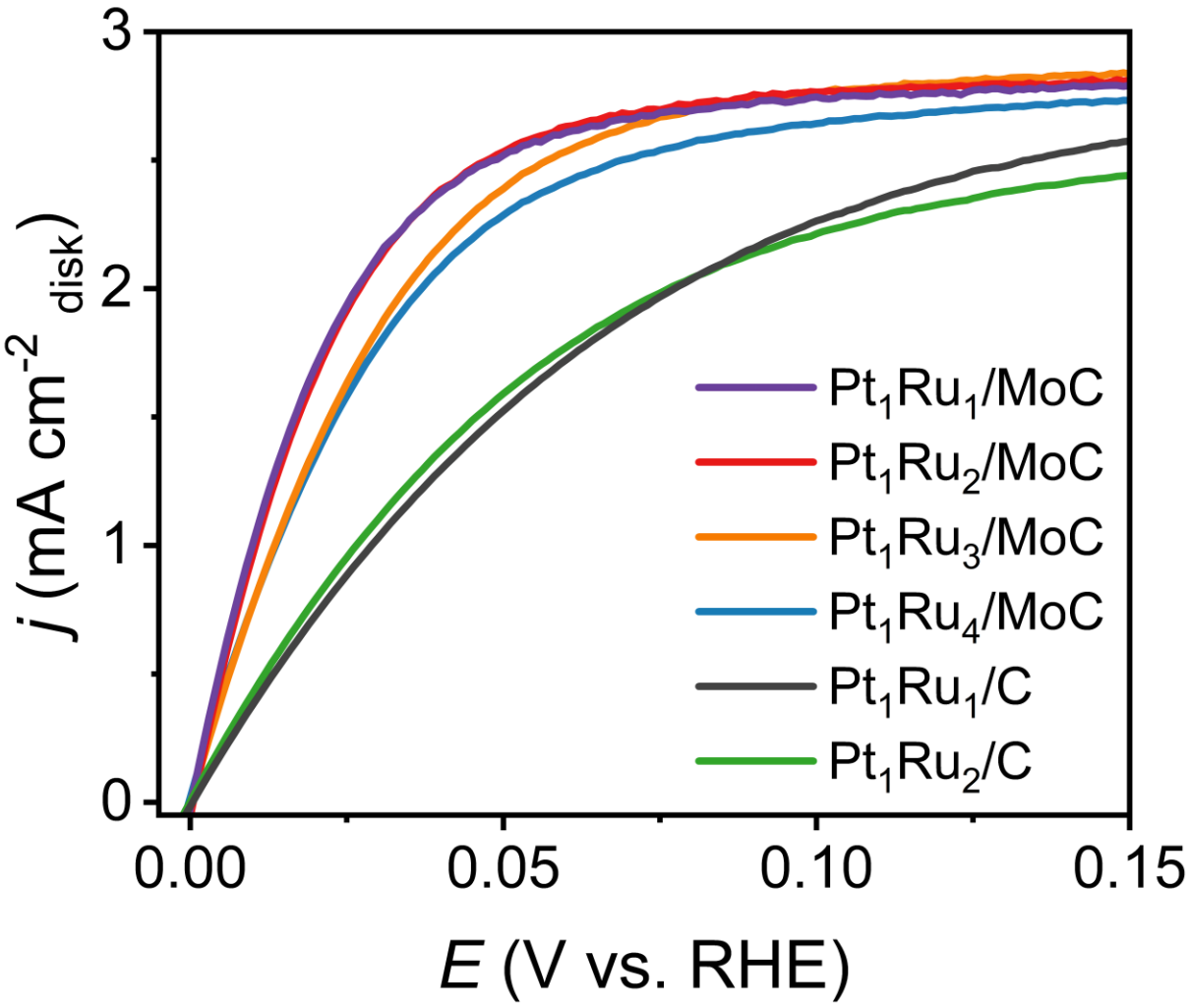

Figure S19. HOR polarization curves in H_2-saturated 0.1 M KOH for PGM/C and PGM/MoC catalysts at different ratios of PGM.

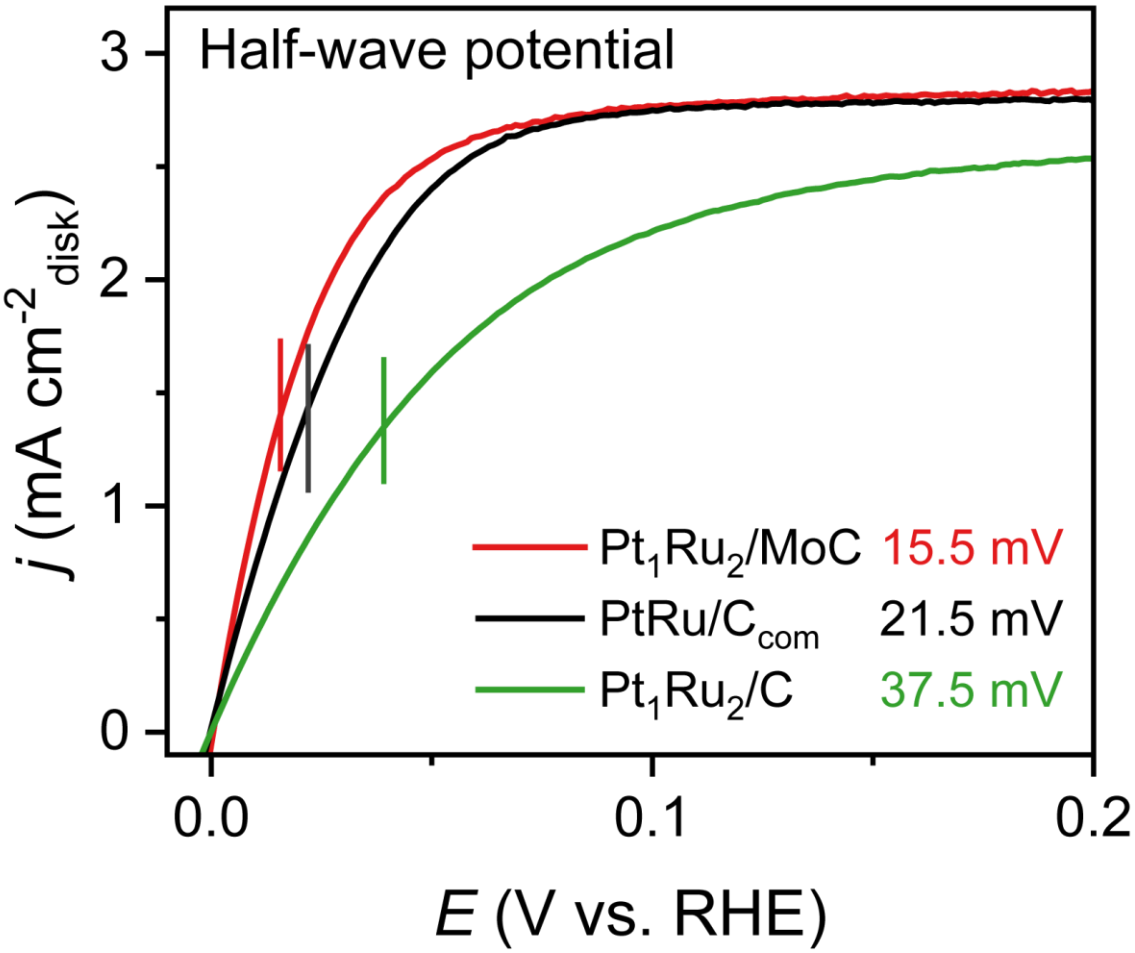

Figure S20. Half-wave potential of Pt_1Ru_2/MoC, PtRu/C_{com} and Pt_1Ru_2/C.

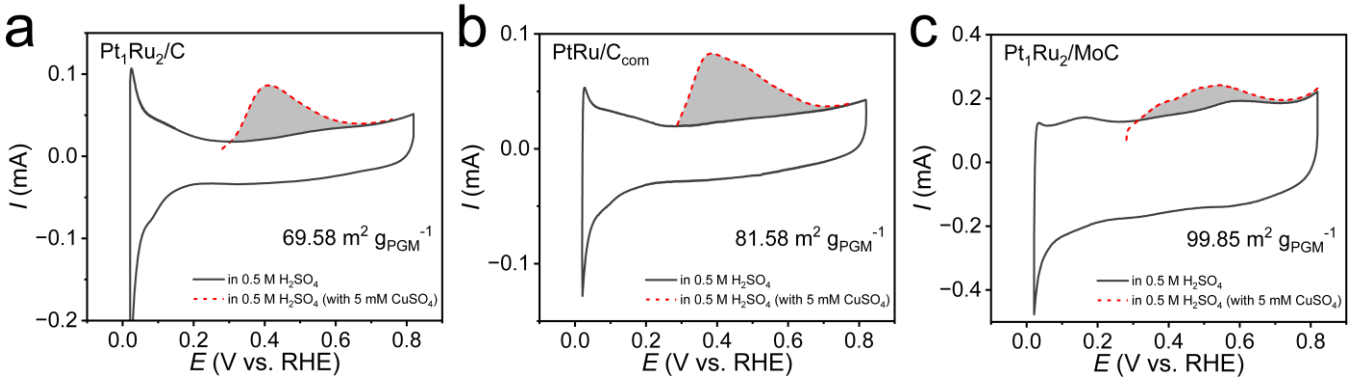

Figure S21. The Cu stripping curves of (a) Pt_1Ru_2/C; (b) $PtRu/C_{com}$ and (c) Pt_1Ru_2/MoC.

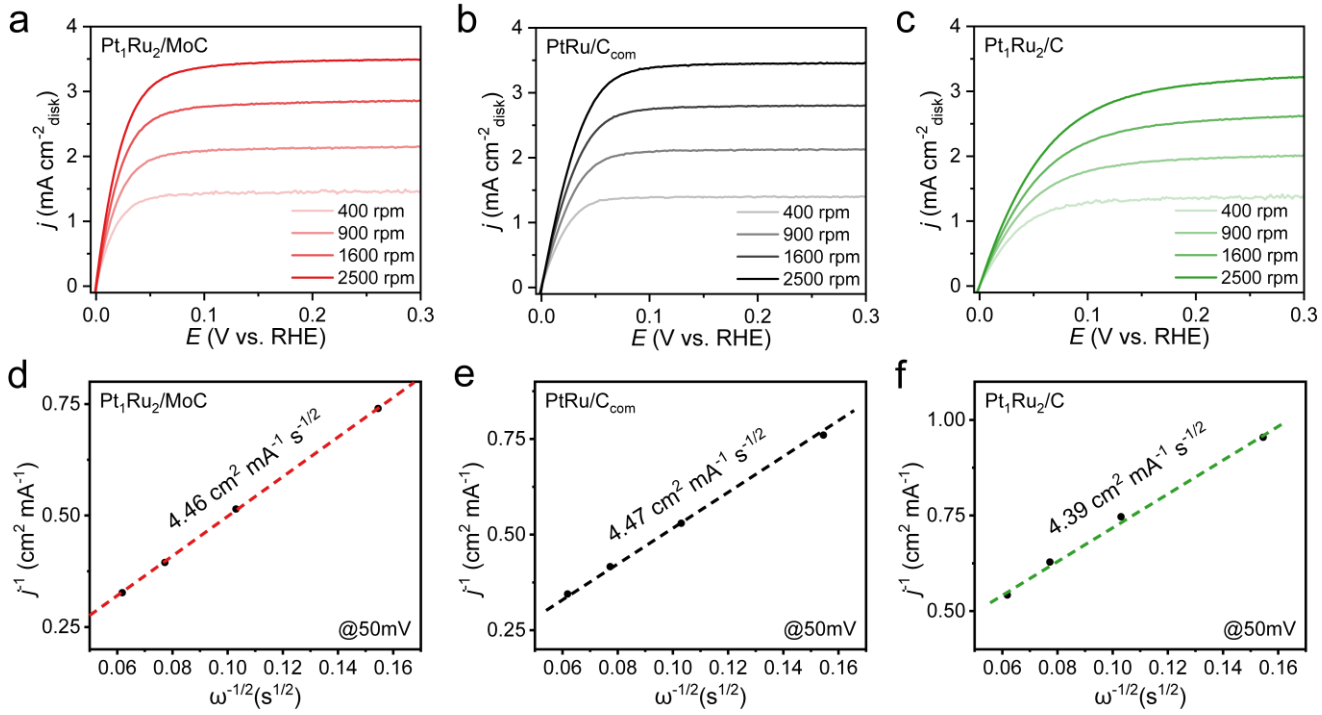

Figure S22. HOR polarization curves in H_2-saturated 0.1 M KOH at the rotating speeds varied from 400 to 2500 rpm of (a) Pt_1Ru_2/MoC, (b) PtRu/C_{com} and (c) Pt_1Ru_2/C. Koutecky-Levich plot at an overpotential of 50 mV of (d) Pt_1Ru_2/MoC, (e) PtRu/C_{com} and (f) Pt_1Ru_2/C.

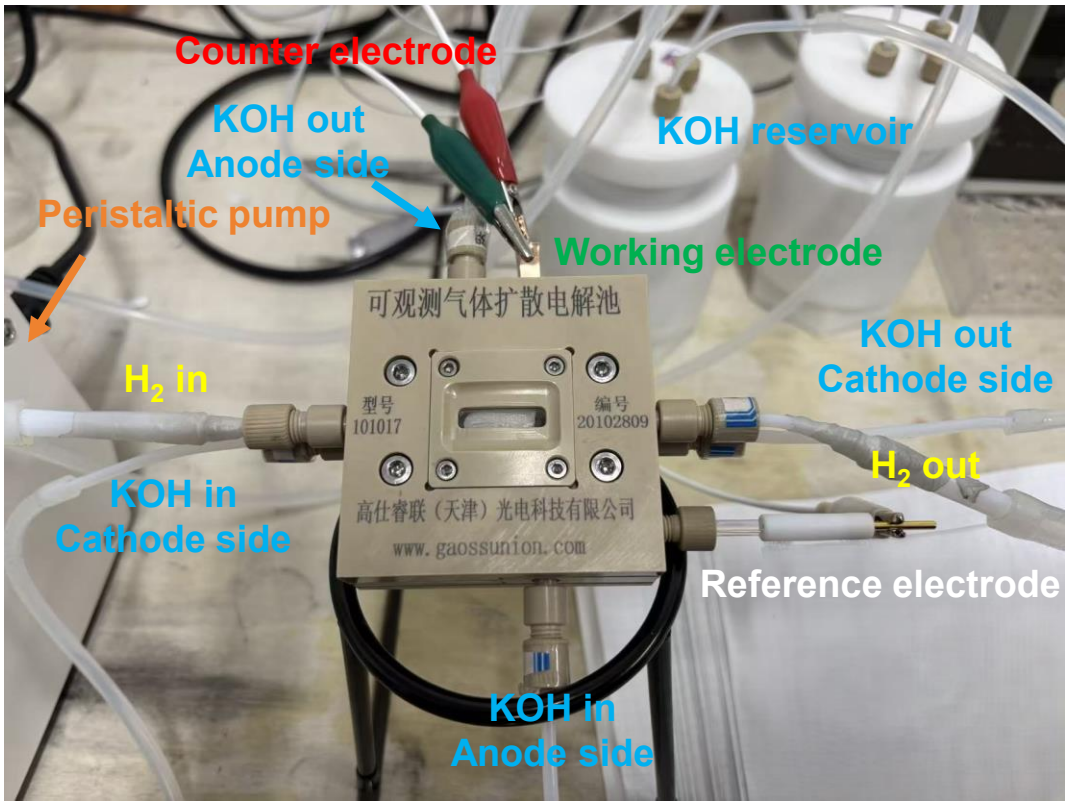

Figure S23. The GDE configuration for alkaline HOR measurements. Key components are labeled to illustrate the electrolyte circulation and cell configuration.

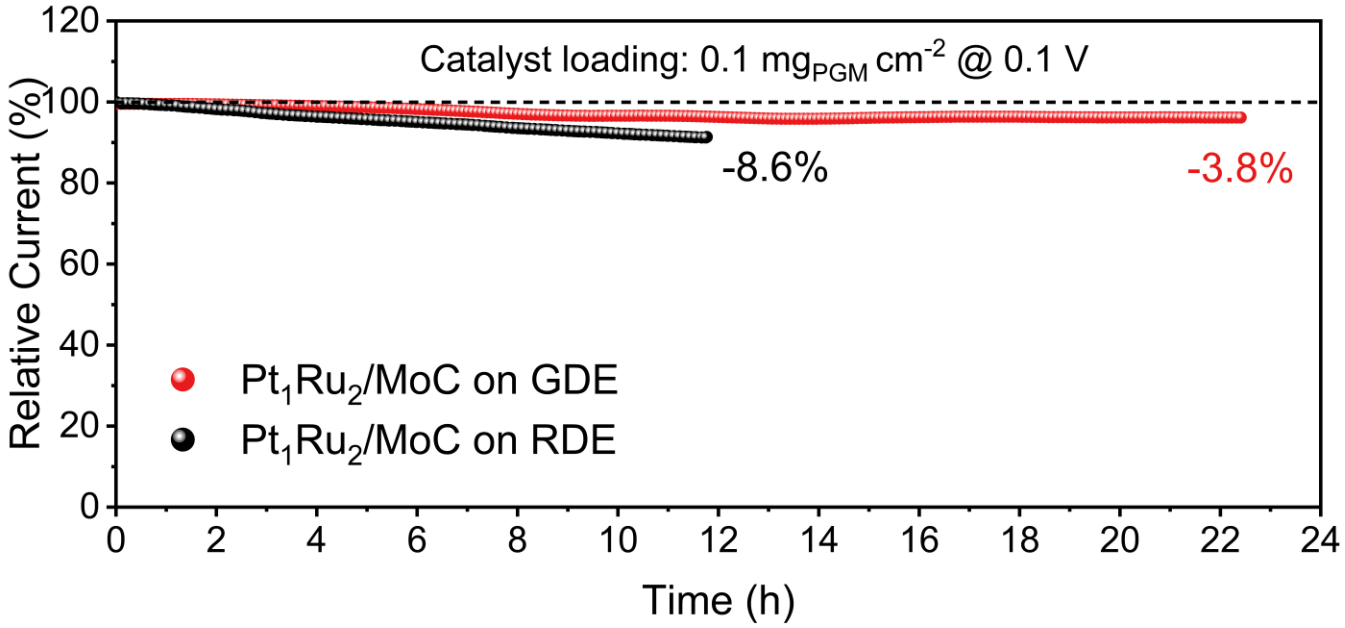

Figure S24. Chronoamperometry tests of Pt_1Ru_2/MoC on RDE and GDE with the same loading (0.1 $mg_{PGM}\,cm^{-2}$).

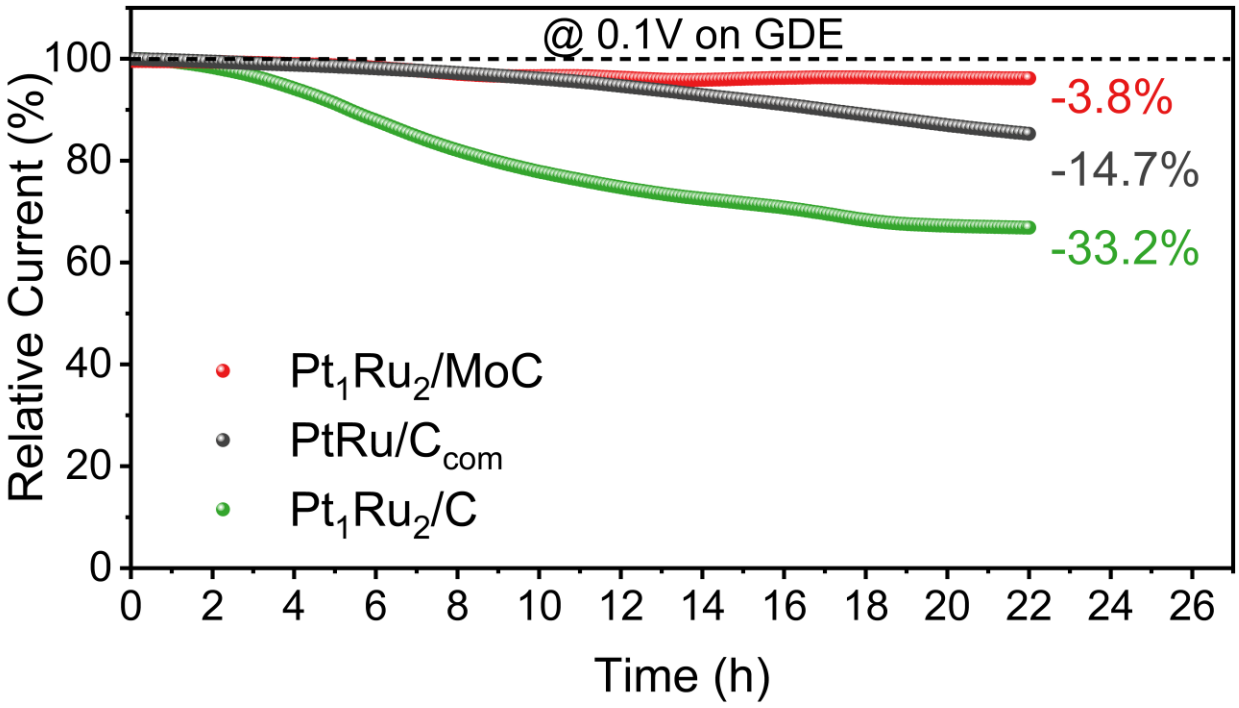

Figure S25. Chronoamperometry tests on GDE of Pt_1Ru_2/MoC, PtRu/C_{com} and Pt_1Ru_2/C with the same loading (0.1 $mg_{PGM}\,cm^{-2}$).

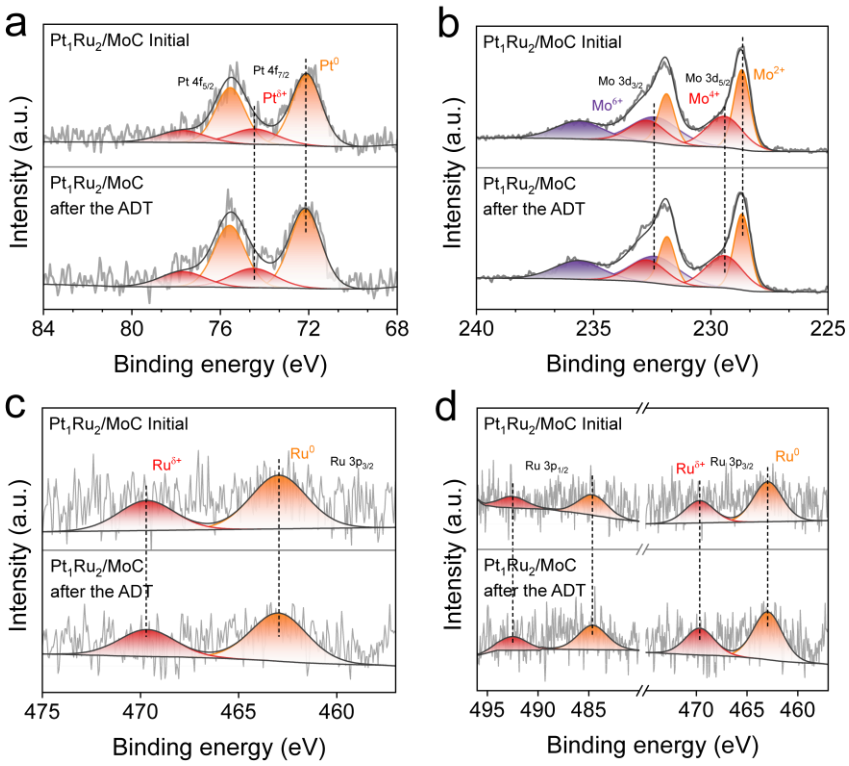

Figure S26. XPS spectra of Pt_1Ru_2/MoC before and after the ADT. (a) Pt 4f XPS spectra. (b) Mo 3d XPS spectra. (c, d) Ru 3p XPS spectra.

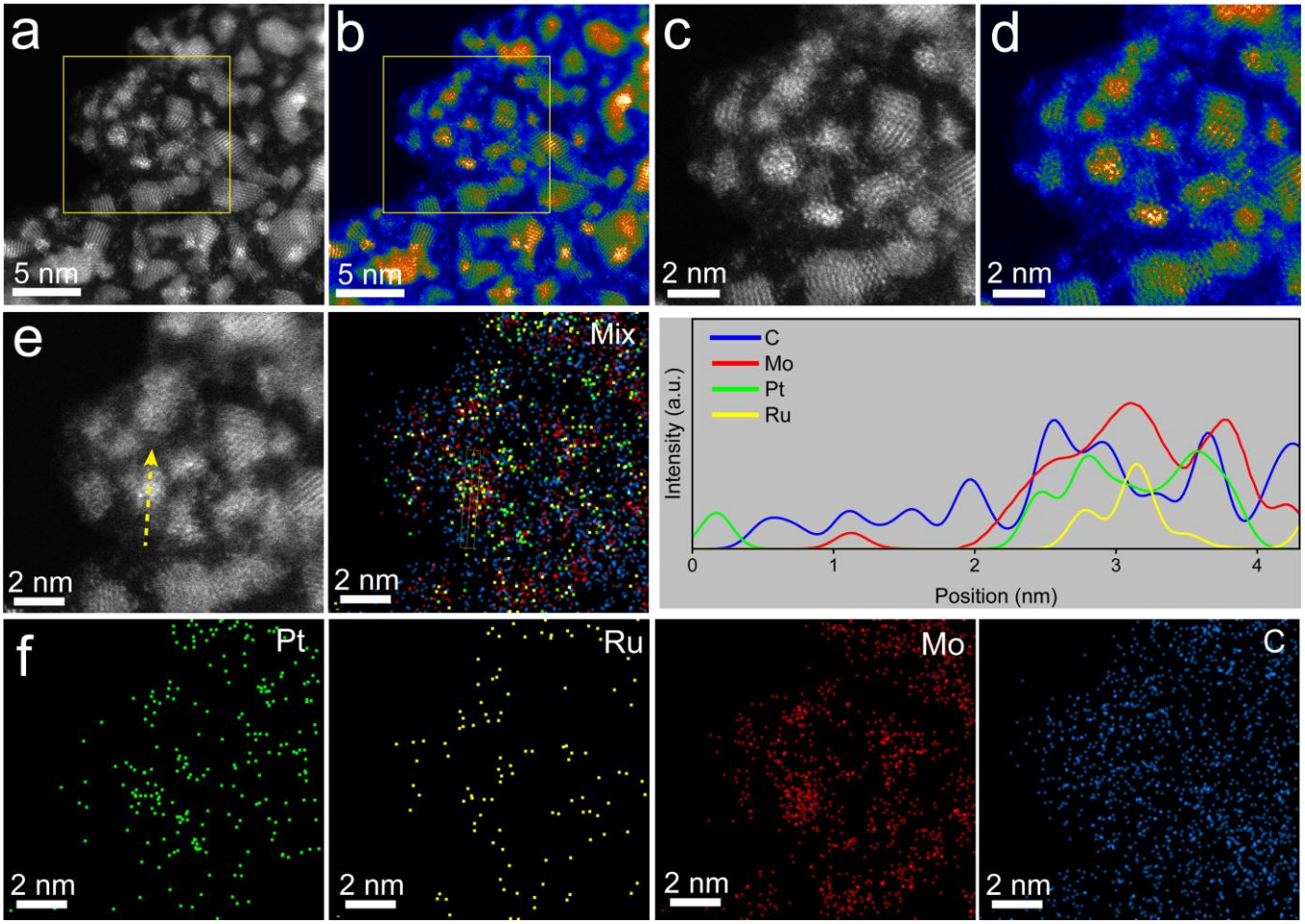

Figure S27. STEM characterization of Pt_1Ru_2/MoC before the ADT. (a) AC-HAADF-STEM image. (b) Corresponding grayscale AC-HAADF-STEM image (color model: temperature). (c) Enlarged AC-HAADF-STEM image. (d) Corresponding enlarged grayscale AC-HAADF-STEM image (color model: temperature). (e) EDS Line Scan images and results. (f) Enlarged STEM EDS elemental mapping images.

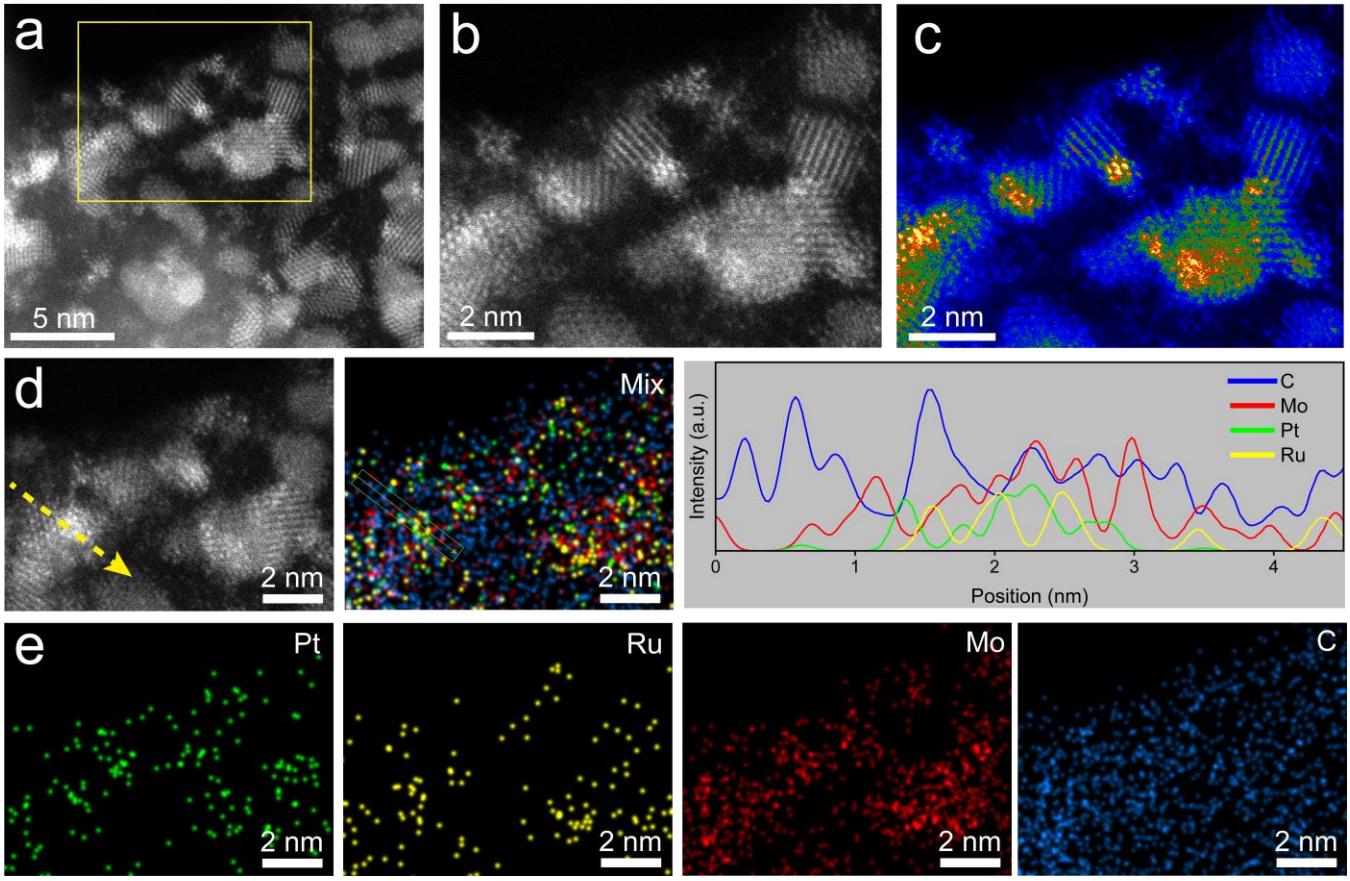

Figure S28. STEM characterization of Pt_1Ru_2/MoC in another representative region before the ADT. (a) AC-HAADF-STEM image. (b) Enlarged AC-HAADF-STEM image. (c) Corresponding enlarged grayscale AC-HAADF-STEM image (color model: temperature). (d) EDS Line Scan images and results. (e) Enlarged STEM EDS elemental mapping images.

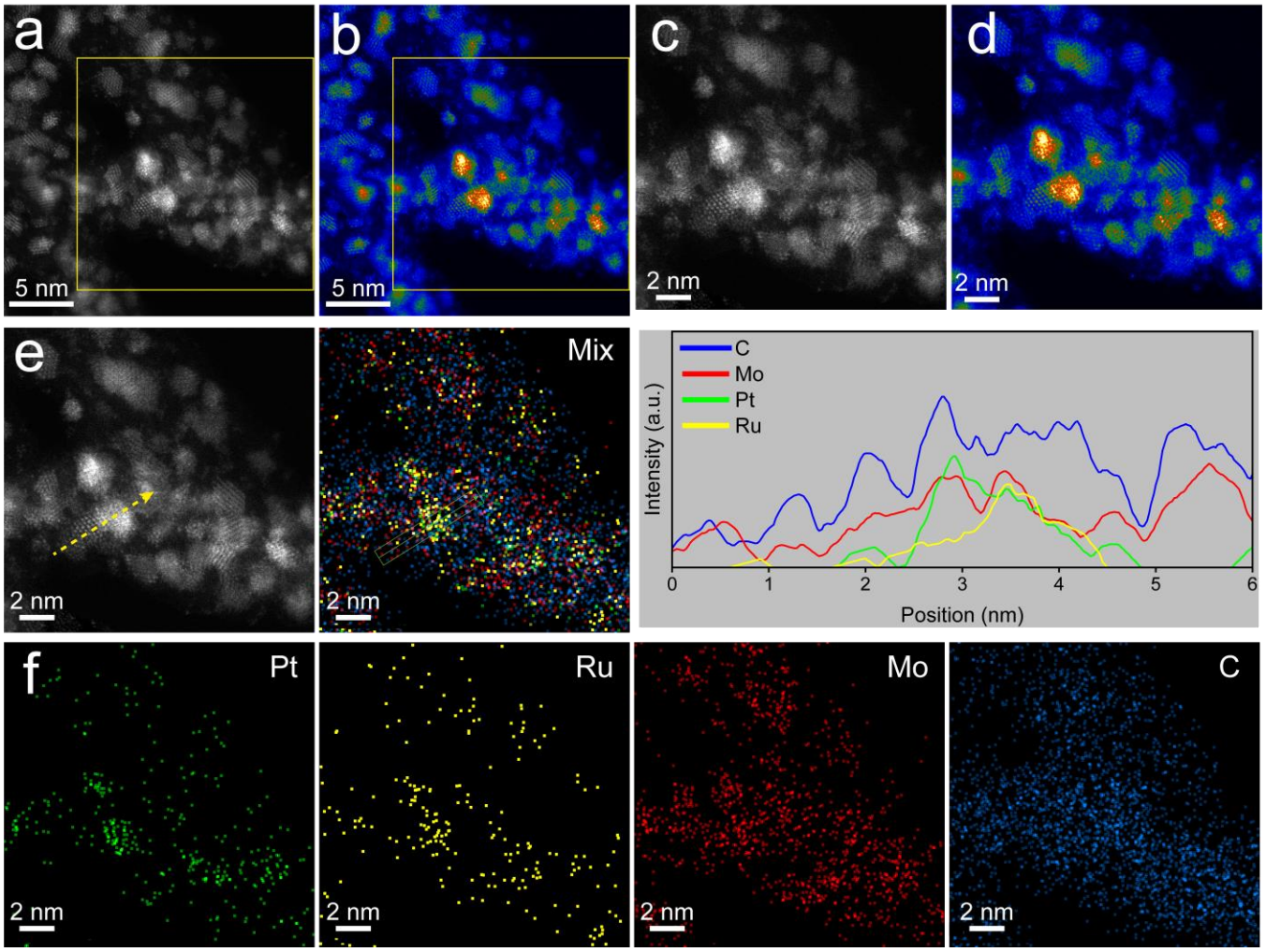

Figure S29. STEM characterization of Pt_1Ru_2/MoC after the ADT. (a) AC-HAADF-STEM image. (b) Corresponding grayscale AC-HAADF-STEM image (color model: temperature). (c) Enlarged AC-HAADF-STEM image. (d) Corresponding enlarged grayscale AC-HAADF-STEM image (color model: temperature). (e) EDS Line Scan images and results. (f) Enlarged STEM EDS elemental mapping images.

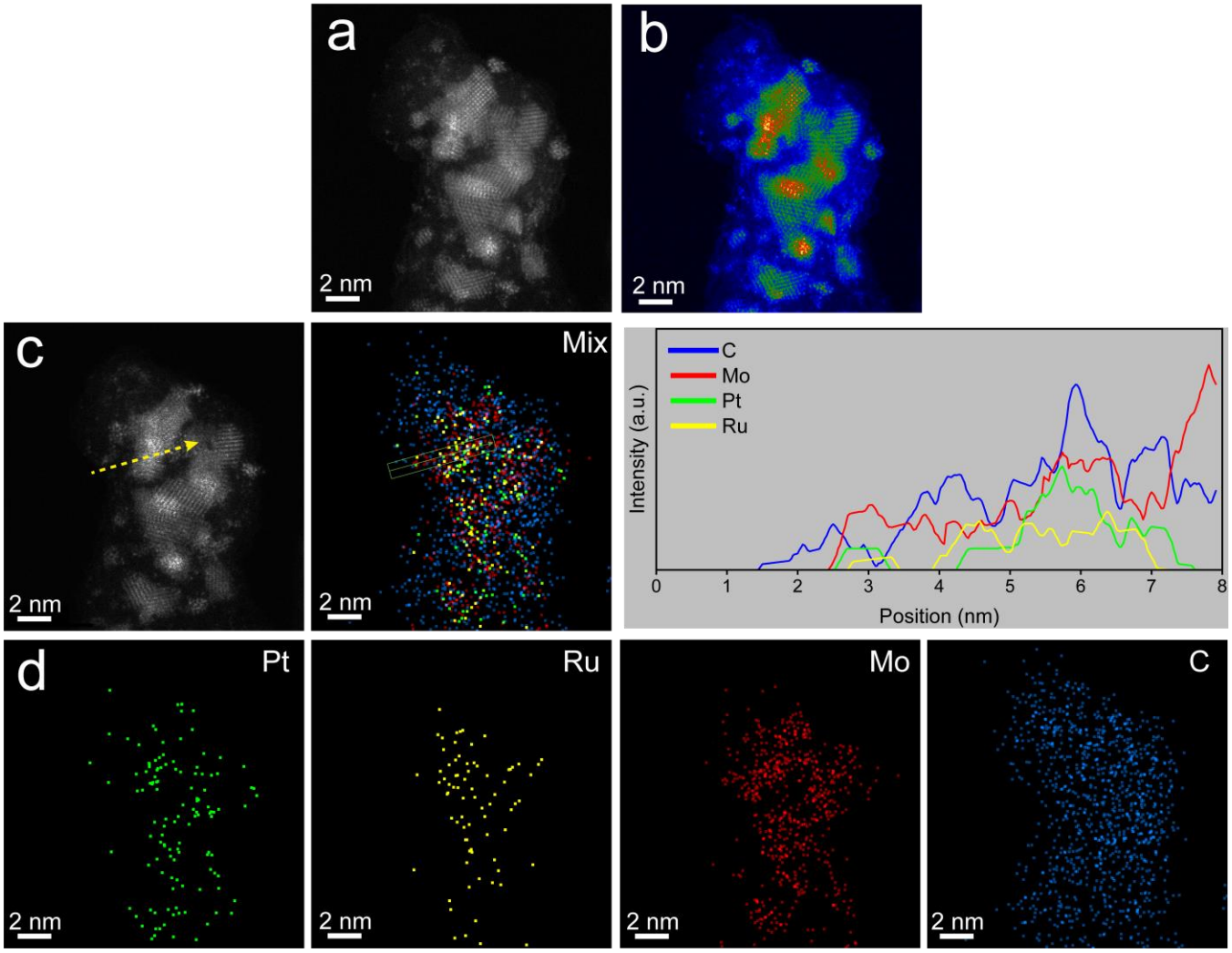

Figure S30. STEM characterization of Pt_1Ru_2/MoC in another representative region after the ADT. (b) Corresponding grayscale AC-HAADF-STEM image (color model: temperature). (c) EDS Line Scan images and results. (d) STEM EDS elemental mapping images.

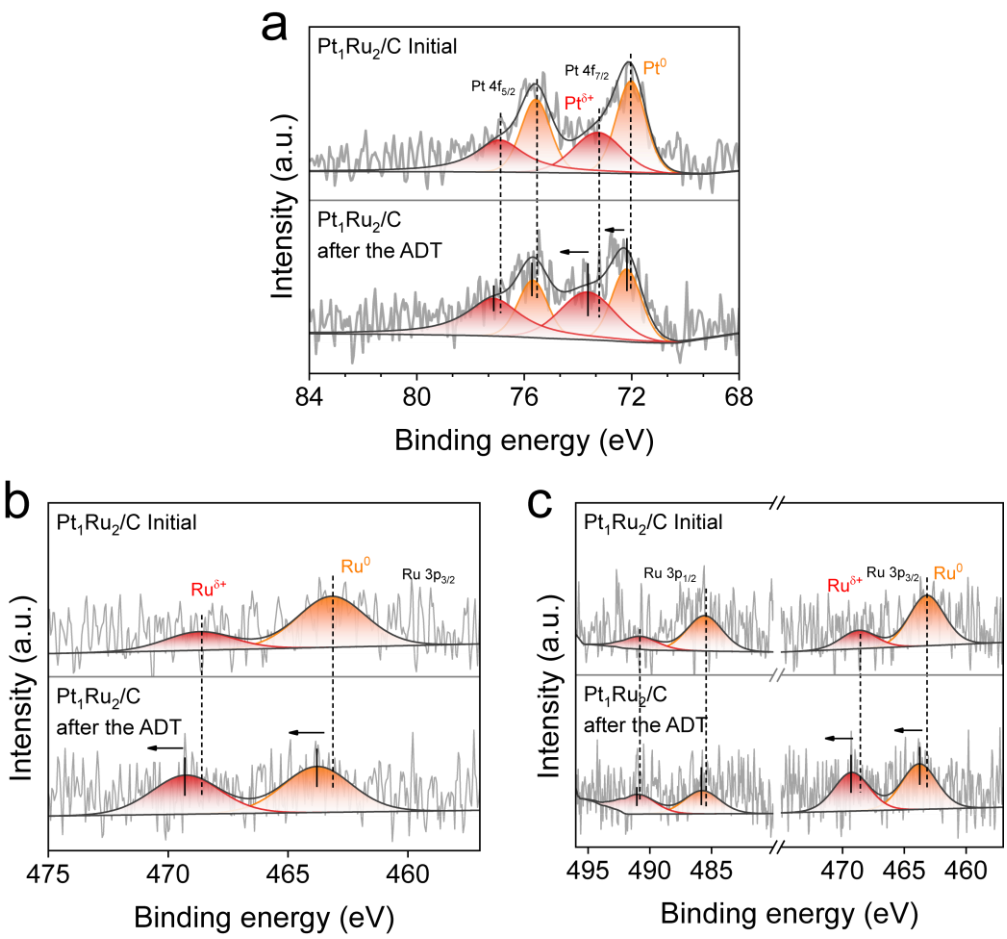

Figure S31. XPS spectra of Pt_1Ru_2/C before and after the ADT. (a) Pt 4f XPS spectra. (b, c) Ru 3p XPS spectra.

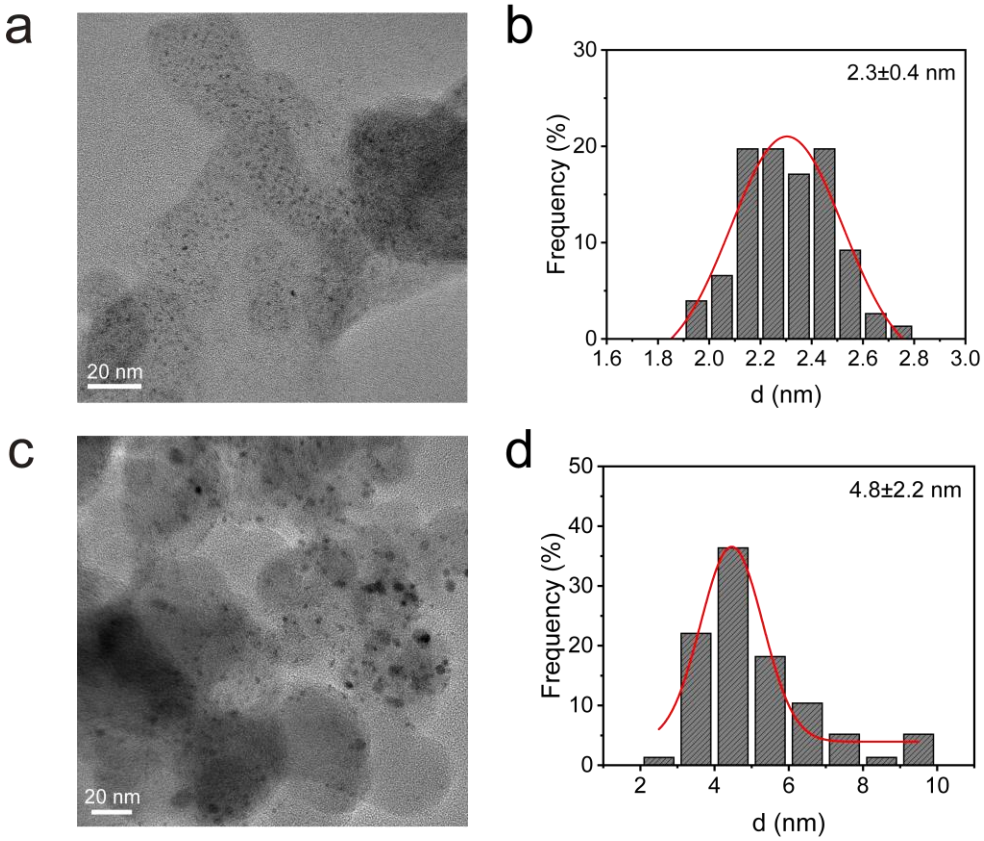

Figure S32. (a) TEM image and (b) size distribution of Pt_1Ru_2/C before the ADT. (c) TEM image and (d) size distribution of Pt_1Ru_2/C after the ADT.

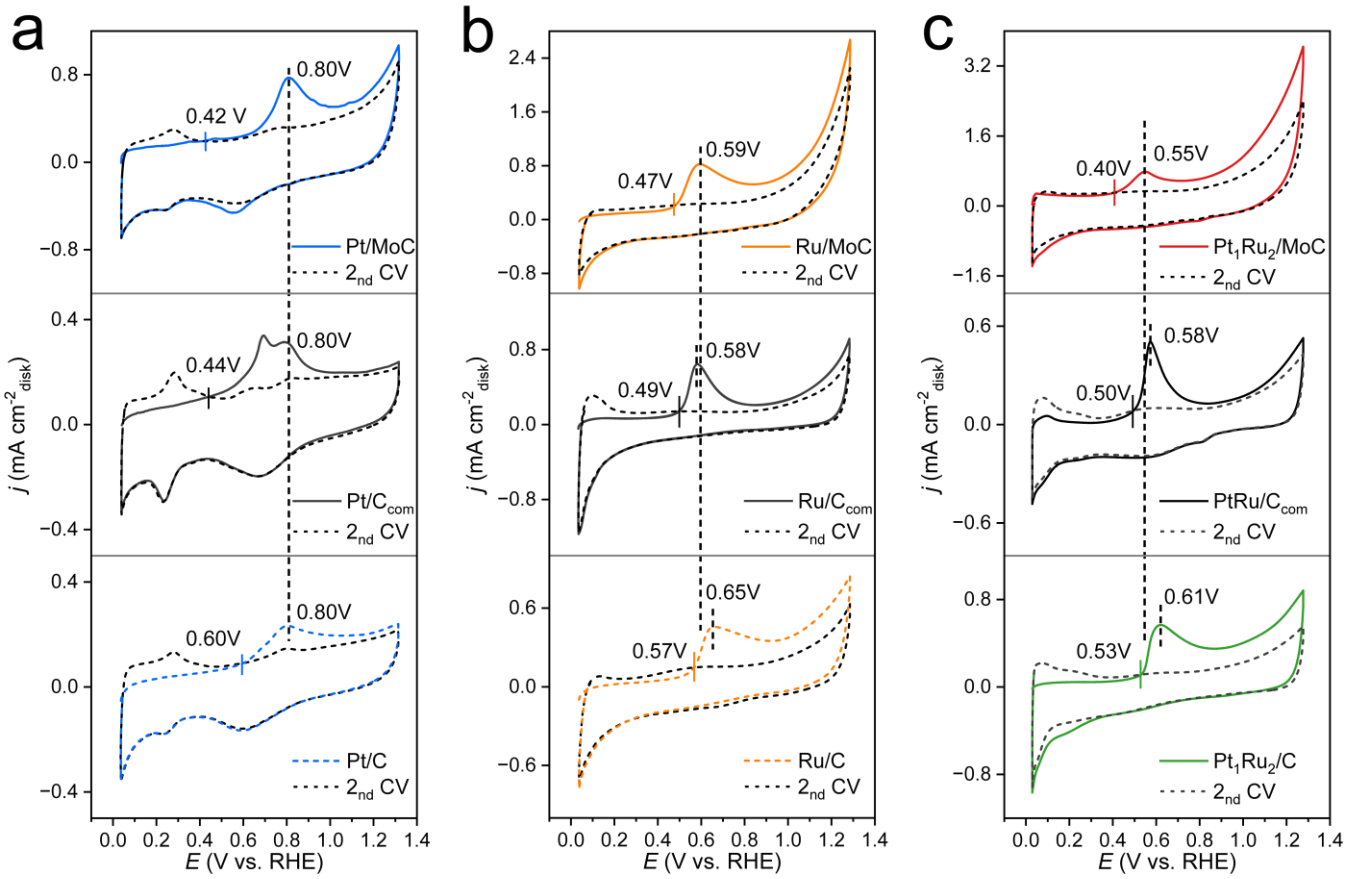

Figure S33. CO stripping voltammetry curves (solid line) with CV background in N_2-saturated 0.1 M KOH (dash line) of different catalysts.

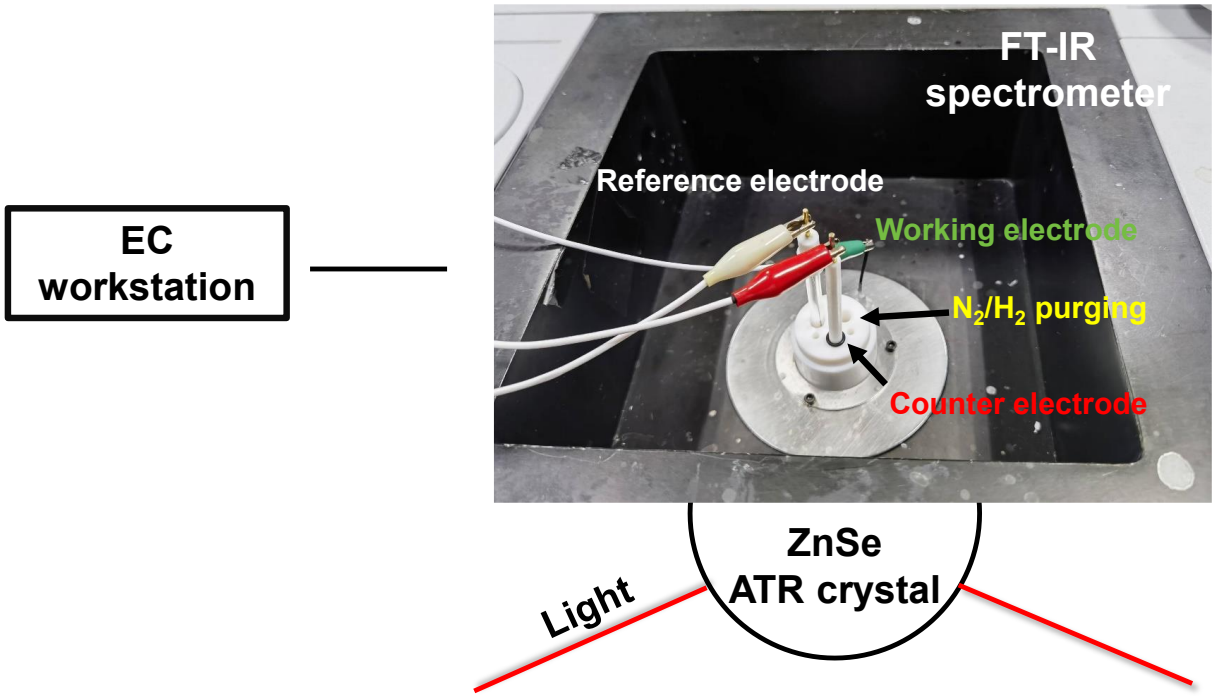

Figure S34. The in-situ ATR-SEIRAS experimental setup. The catalyst ink is dropped and dried on the surface of ZnSe crystal, which is located at the bottom of the electrochemical cell.

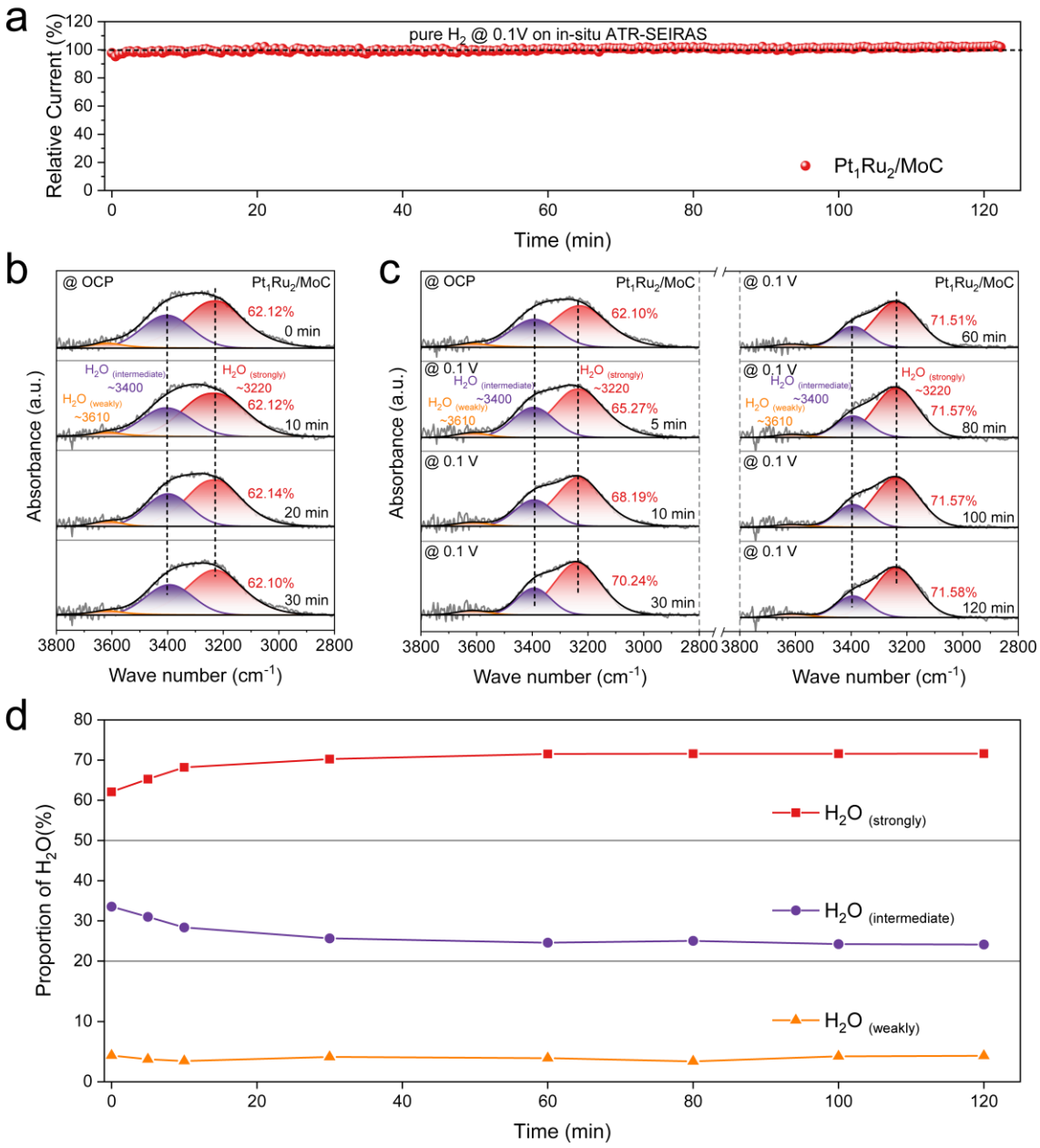

Figure S35. In-situ ATR-SEIRAS spectra of Pt_1Ru_2/MoC under durability-relevant alkaline HOR conditions. (a) Chronoamperometric response recorded during in-situ ATR-SEIRAS measurements at 0.1 V. In-situ ATR-SEIRAS spectra in the OH stretching region at (b) OCP and (c) 0.1 V. (d) Quantitative evolution of strongly, intermediate, and weakly hydrogen-bonded water components as a function of operation time.

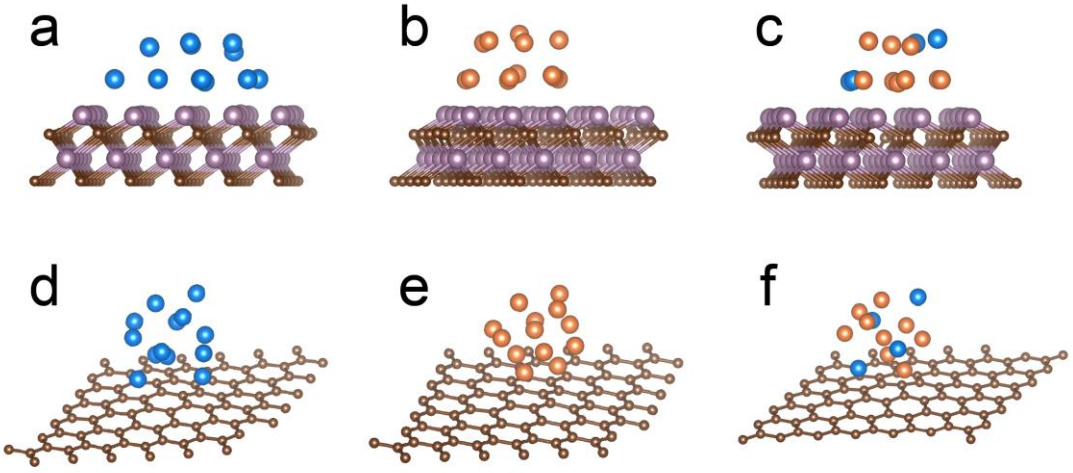

Figure S36. Optimized structural models of (a) Pt/MoC; (b) Ru/MoC; (c) Pt_1Ru_2/MoC; (d) Pt/C; (e) Ru/C; (f) Pt_1Ru_2/C.

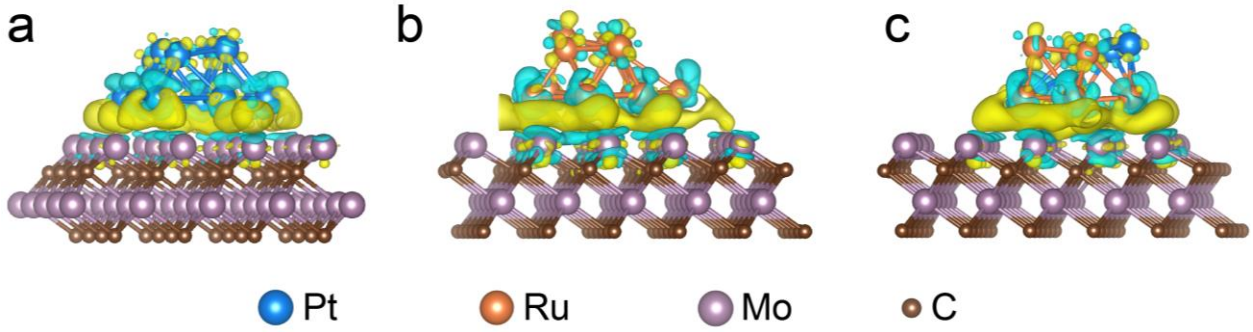

Figure S37. The differential charge density of (a) Pt/MoC; (b) Ru/MoC; (c) Pt_1Ru_2/MoC. Yellow and cyan represent increased and decreased charge distributions, respectively.

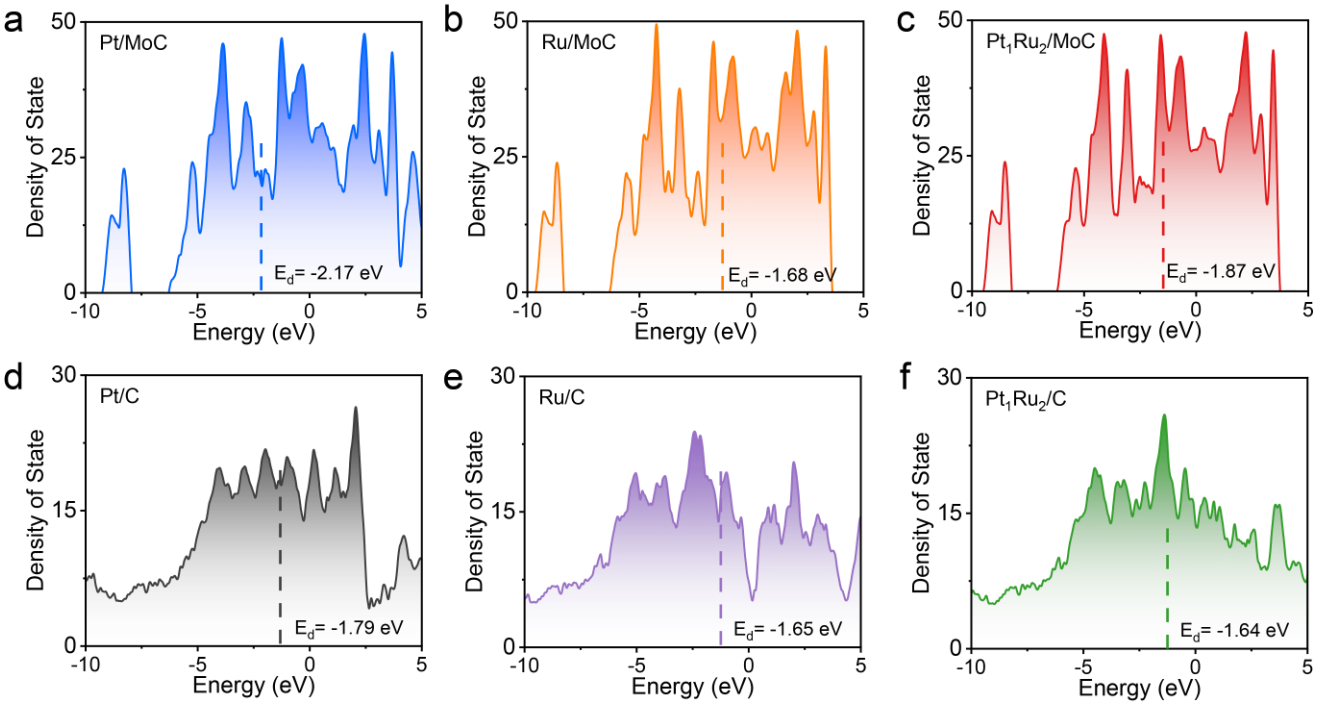

Figure S38. The DOS for the different catalysts loading on MoC and carbon support with the values of d-band center, respectively: (a) Pt/MoC; (b) Ru/MoC; (c) Pt_1Ru_2/MoC; (d) Pt/C; (e) Ru/C; (f) Pt_1Ru_2/C.

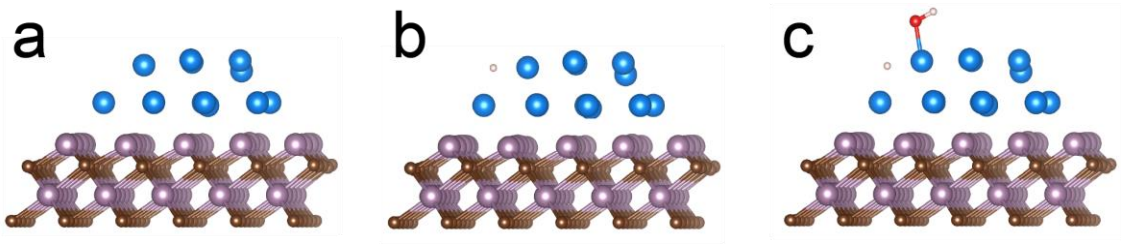

Figure S39. Optimized atomic structure of the Pt/MoC surface under different conditions: (a) pure surface, (b) H adsorption and (c) H and OH adsorption. Colors indicate: blue, Pt; purple, Mo; brown, C; pink, H; red, O.

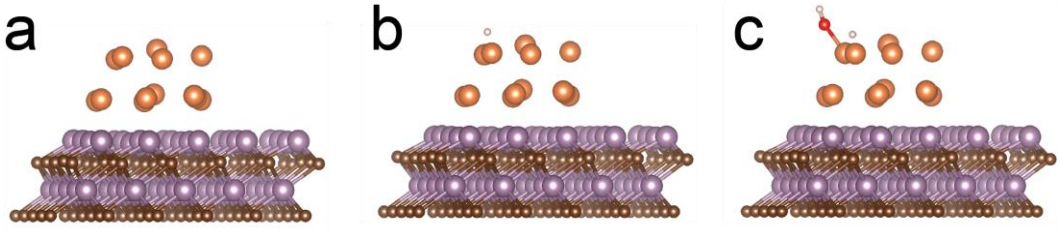

Figure S40. Optimized atomic structure of the Ru/MoC surface under different conditions: (a) pure surface, (b) H adsorption and (c) H and OH adsorption. Colors indicate: orange, Ru; purple, Mo; brown, C; pink, H; red, O.

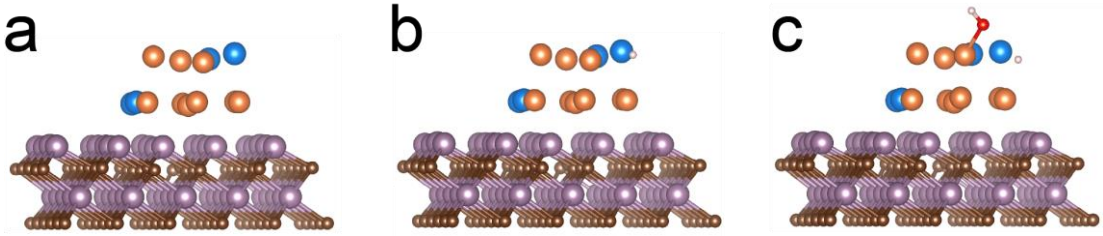

Figure S41. Optimized atomic structure of the Pt_1Ru_2/MoC surface under different conditions: (a) pure surface (b) H adsorption, and (c) H and OH adsorption. Colors indicate: blue, Pt; orange, Ru; purple, Mo; brown, C; pink, H; red, O.

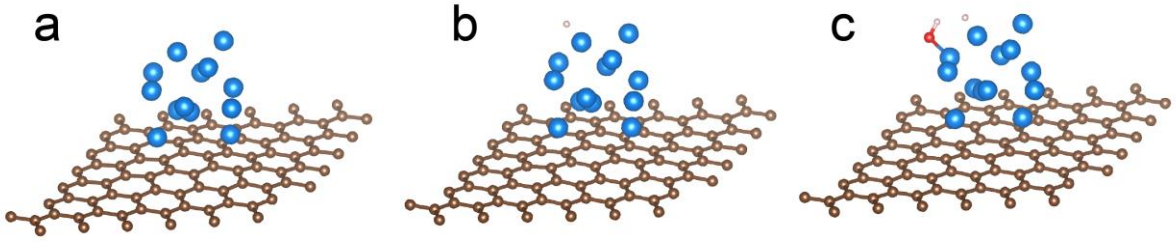

Figure S42. Optimized atomic structure of the Pt/C surface under different conditions: (a) pure surface, (b) H adsorption and (c) H and OH adsorption. Colors indicate: blue, Pt; brown, C; pink, H; red, O.

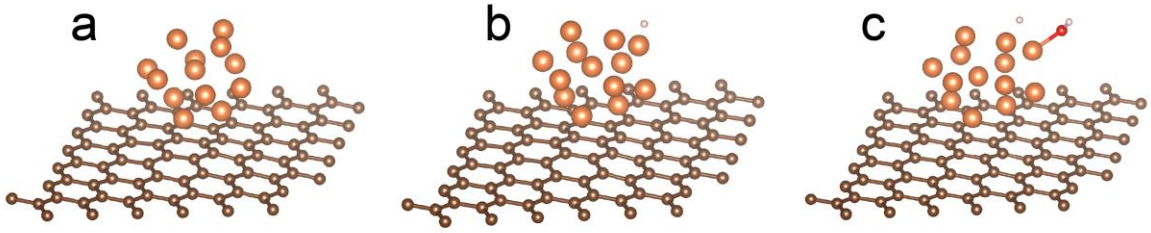

Figure S43. Optimized atomic structure of the Ru/C surface under different conditions: (a) pure surface, (b) H adsorption and (c) H and OH adsorption. Colors indicate: orange, Ru; brown, C; pink, H; red, O.

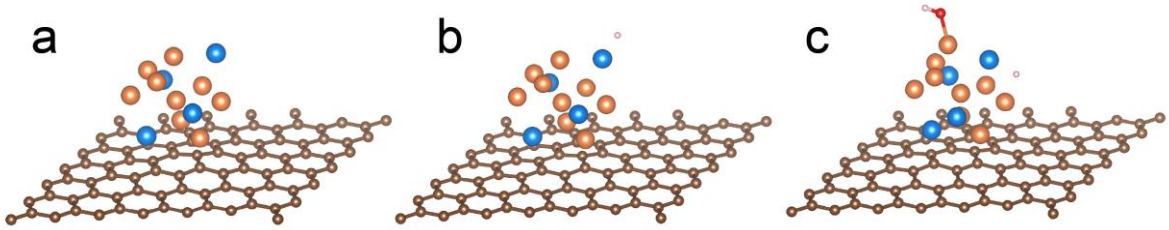

Figure S44. Optimized atomic structure of the Pt_1Ru_2/C surface under different conditions: (a) pure surface, (b) H adsorption and (c) H and OH adsorption. Colors indicate: blue, Pt; orange, Ru; brown, C; pink, H; red, O.

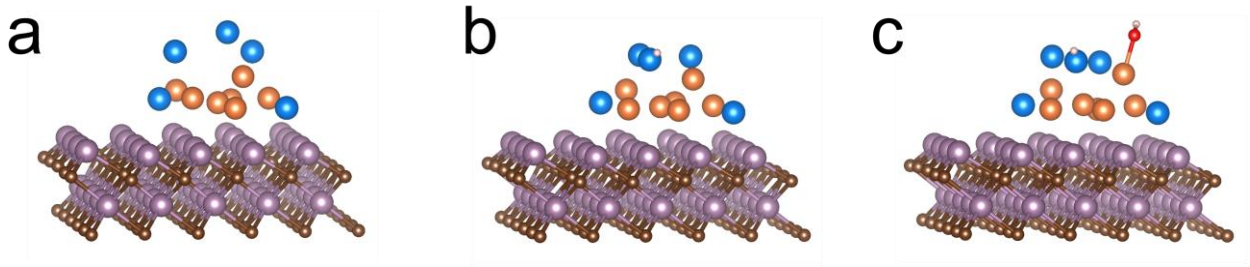

Figure S45. Optimized atomic structure of the Pt_1Ru_1/MoC surface under different conditions: (a) pure surface, (b) H adsorption and (c) H and OH adsorption. Colors indicate: blue, Pt; orange, Ru; brown, C; pink, H; red, O.

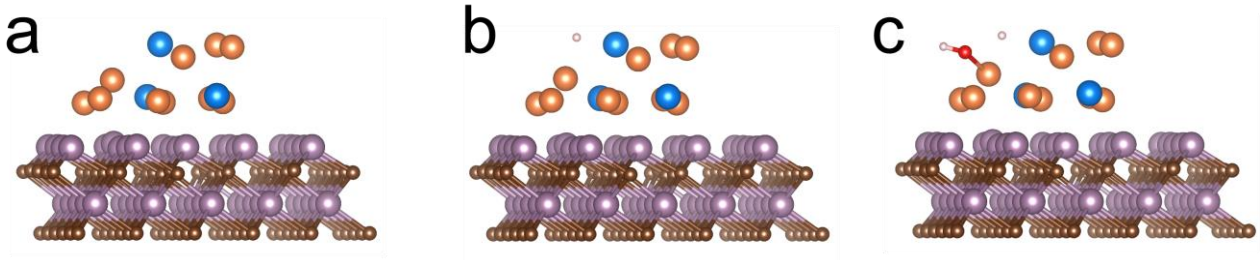

Figure S46. Optimized atomic structure of the Pt_1Ru_3/MoC surface under different conditions: (a) pure surface, (b) H adsorption and (c) H and OH adsorption. Colors indicate: blue, Pt; orange, Ru; brown, C; pink, H; red, O.

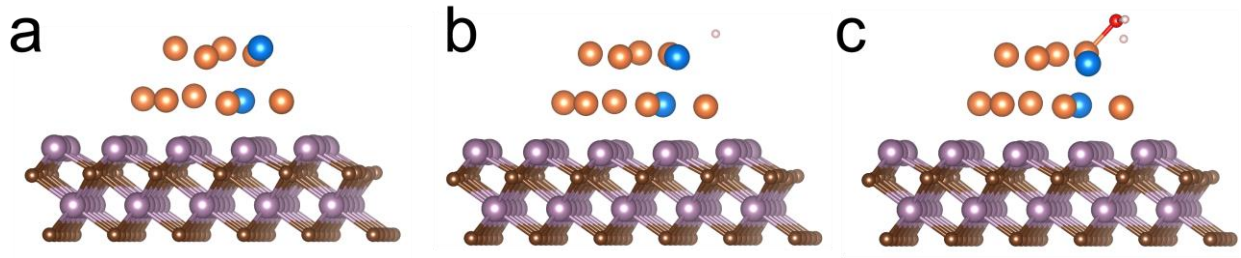

Figure S47. Optimized atomic structure of the Pt_1Ru_4/MoC surface under different conditions: (a) pure surface, (b) H adsorption and (c) H and OH adsorption. Colors indicate: blue, Pt; orange, Ru; brown, C; pink, H; red, O.

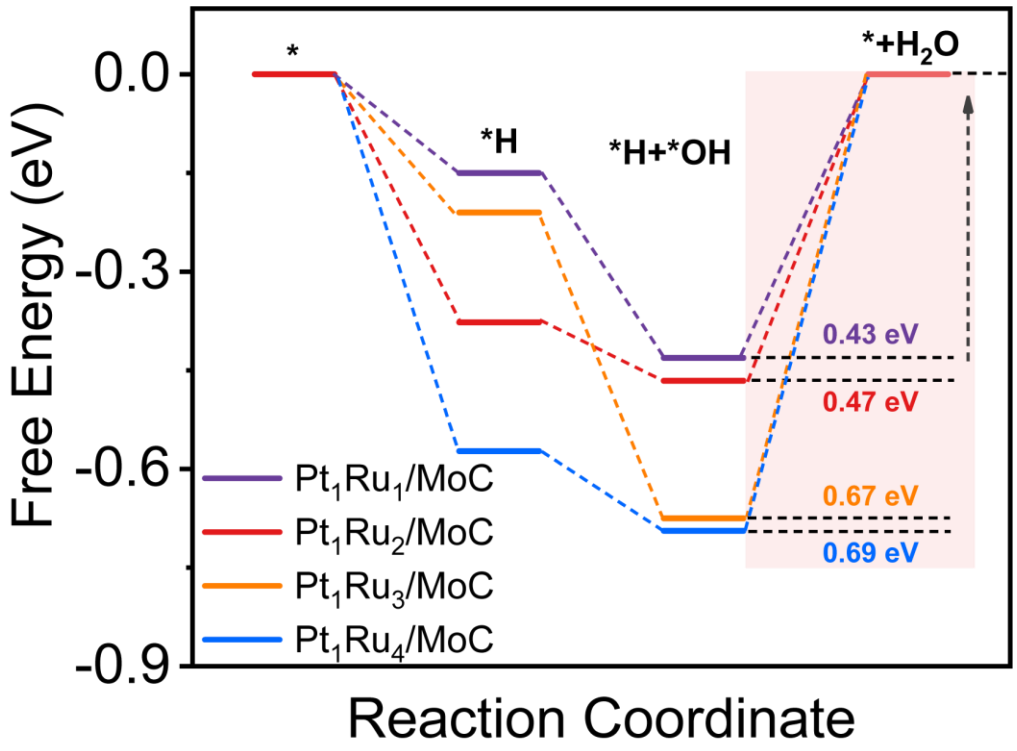

Figure S48. The Gibbs free energies of reaction pathways for HOR on Pt_1Ru_1/MoC, Pt_1Ru_2/MoC, Pt_1Ru_3/MoC and Pt_1Ru_4/MoC, respectively.

Note: The additional Gibbs free energies of reaction pathways for different Pt/Ru ratio reveal that Pt_1Ru_1/MoC (0.43 eV) and Pt_1Ru_2/MoC (0.47 eV) exhibit comparable RDS barriers, both of which are significantly lower than those of Pt_1Ru_3/MoC (0.67 eV) and Pt_1Ru_4/MoC (0.69 eV). Together with the experimentally measured HOR polarization curves (Figure S19), these results indicate that optimal HOR activity is achieved within a narrow compositional window rather than at a single, well-defined stoichiometric ratio. To achieve a more favorable balance between catalytic performance and economic viability, Pt_1Ru_2/MoC was therefore selected instead of Pt_1Ru_1/MoC as the representative catalyst for the systematic investigation presented in this work.

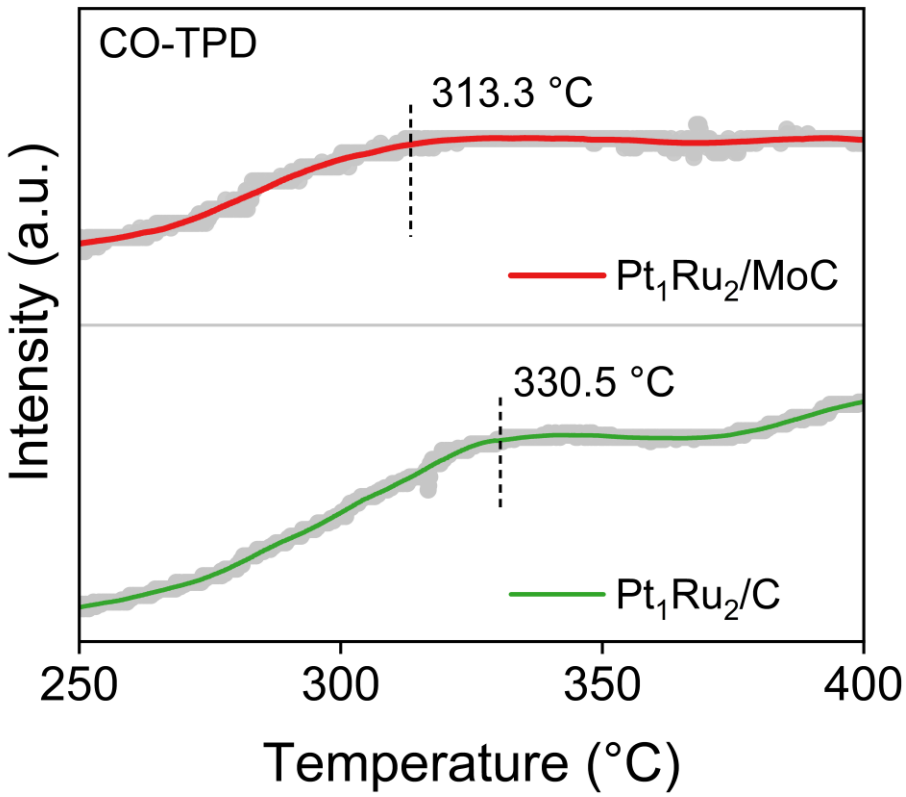

Figure S49. CO temperature programed desorption (CO-TPD) curves of Pt_1Ru_2/MoC and Pt_1Ru_2/C.

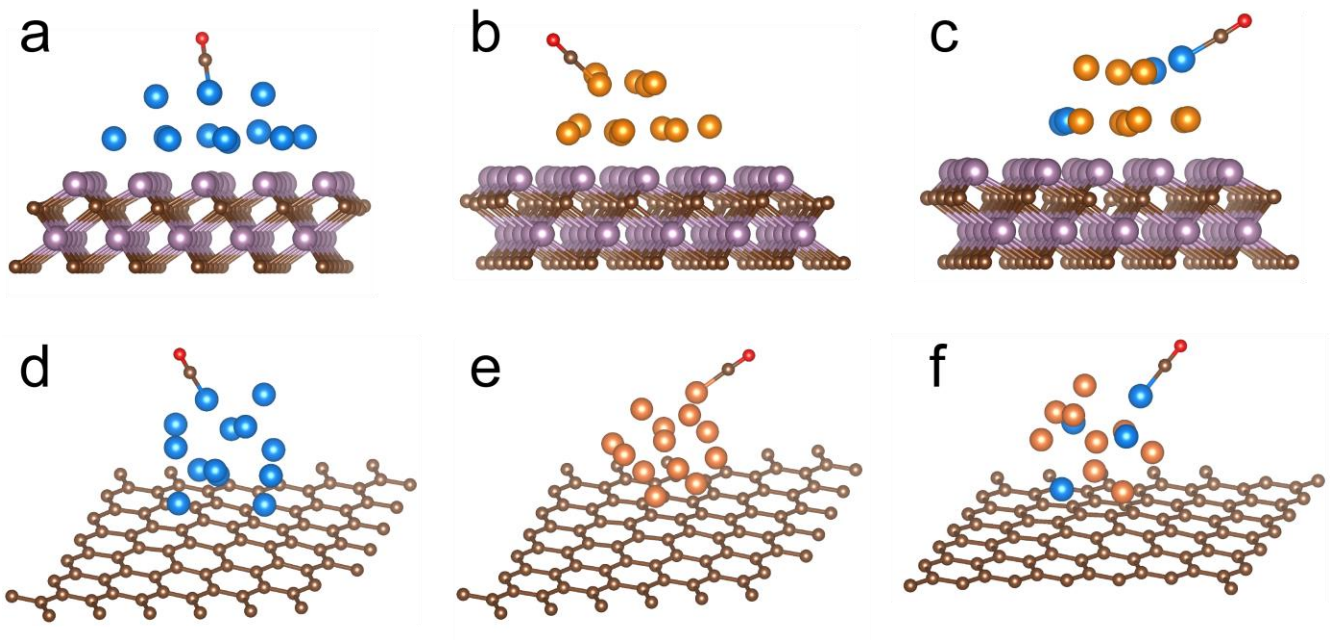

Figure S50. Optimized structural models of (a) Pt/MoC; (b) Ru/MoC; (c) Pt_1Ru_2/MoC; (d) Pt/C; (e) Ru/C; (f) Pt_1Ru_2/C under CO adsorption. Colors indicate: blue, Pt; orange, Ru; brown, C; red, O.

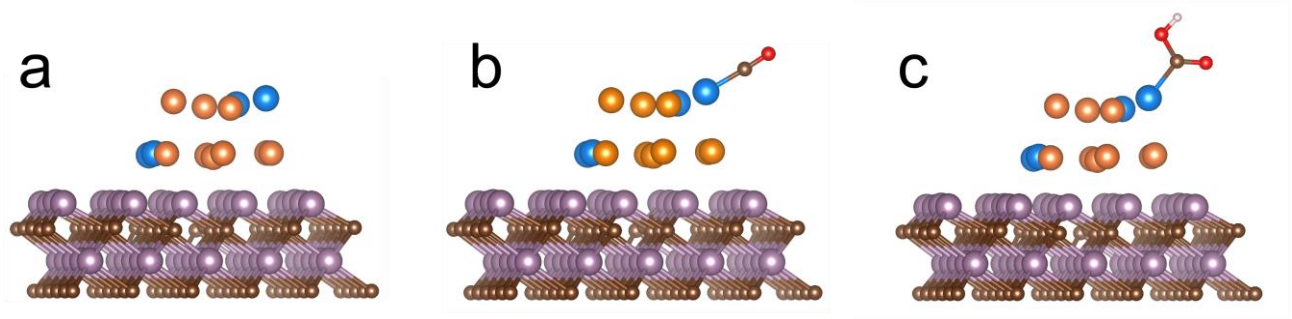

Figure S51. Optimized structure of the Pt_1Ru_2/MoC surface for the CO oxidation pathway: (a) pure surface, (b) CO adsorption and (c) *COOH adsorption. Colors indicate: blue, Pt; orange, Ru; brown, C; pink, H; red, O.

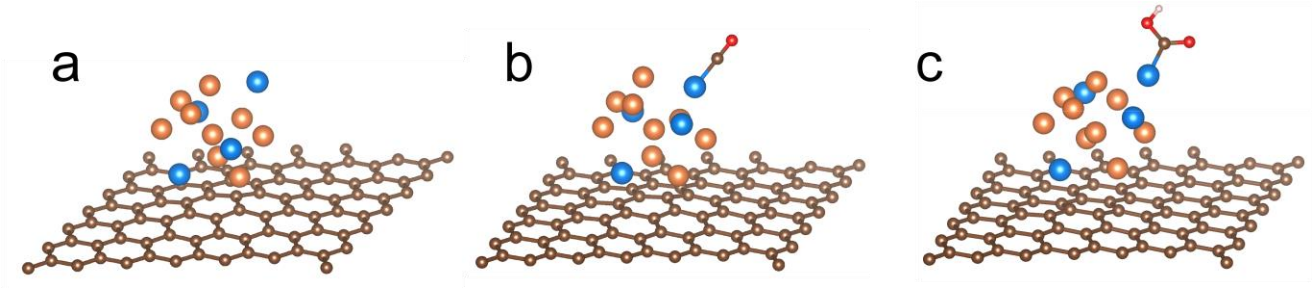

Figure S52. Optimized structure of the Pt_1Ru_2/C surface for the CO oxidation pathway: (a) pure surface, (b) CO adsorption and (c) *COOH adsorption. Colors indicate: blue, Pt; orange, Ru; brown, C; pink, H; red, O.

Table S1. ICP-MS results for chemical compositions in different catalysts.

Catalyst	Pt (wt%)	Ru (wt%)	Mo (wt%)
Pt/MoC	4.01%	-	59.22%
Pt/C	4.59%	-	-
Ru/MoC	-	4.05%	60.40%
Ru/C	-	4.27%	-
Pt_1Ru_2/MoC	2.39%	2.06%	60.80%
Pt_1Ru_2/C	2.59%	1.92%	-

Table S2. Pt 4f XPS spectra fitting parameters for different catalysts.

Catalyst	Pt species	$4f_{7/2}$ BE (eV)	$4f_{5/2}$ BE (eV)	FHWM (eV)	Proportion (%)
Pt/C	Pt^0	71.90	75.24	1.20 (0.5:2.5)	48.68
	$Pt^{\delta+}$	72.96	76.36	2.45 (0.5:2.5)	51.32
Pt_1Ru_2/C	Pt^0	72.34	75.77	1.77 (0.5:3.5)	58.94
	$Pt^{\delta+}$	74.11	77.61	3.50 (0.5:3.5)	41.06
Pt/MoC	Pt^0	72.01	75.39	1.50 (0.5:2.5)	71.33
	$Pt^{\delta+}$	73.63	77.03	2.50 (0.5:2.5)	28.67
Pt_1Ru_2/MoC	Pt^0	72.10	75.56	1.72 (0.5:3.5)	80.09
	$Pt^{\delta+}$	74.53	77.73	2.50 (0.5:3.5)	19.91

Table S3. Ru 3p XPS spectra fitting parameters for different catalysts.

Catalyst	Ru species	$3p_{3/2}$ BE (eV)	$3p_{1/2}$ BE (eV)	FHWM (eV)	Proportion (%)
Ru/C	Ru^0	461.20	483.80	3.5 (0.5:3.5)	72.47
	$Ru^{\delta+}$	465.25	487.20	3.5 (0.5:3.5)	27.53
Pt_1Ru_2/C	Ru^0	460.62	482.58	3.5 (0.5:3.5)	64.41
	$Ru^{\delta+}$	464.20	486.16	3.5 (0.5:3.5)	35.59
Ru/MoC	Ru^0	461.42	483.35	3.5 (0.5:3.5)	72.62
	$Ru^{\delta+}$	466.43	488.38	3.5 (0.5:3.5)	27.38
Pt_1Ru_2/MoC	Ru^0	461.59	483.40	3.5 (0.5:3.5)	66.62
	$Ru^{\delta+}$	466.61	488.56	3.5 (0.5:3.5)	33.38

Table S4. Mo 3d XPS spectra fitting parameters for different catalysts.

Catalyst	Mo species	$3d_{5/2}$ BE (eV)	$3d_{3/2}$ BE (eV)	FHWM (eV)	Proportion (%)
MoC	Mo^{2+}	228.76	231.93	0.87 (0.5:2.5)	37.24
	Mo^{4+}	229.45	232.66	1.82 (0.5:2.5)	33.32
	Mo^{6+}	232.35	235.56	2.46 (0.5:2.5)	29.44
Pt/MoC	Mo^{2+}	228.62	231.78	0.85 (0.5:2.5)	38.47
	Mo^{4+}	229.41	232.63	1.84 (0.5:2.5)	31.39
	Mo^{6+}	232.32	235.60	2.20 (0.5:2.5)	30.14
Ru/MoC	Mo^{2+}	228.62	231.79	0.92 (0.5:2.5)	44.00
	Mo^{4+}	229.50	232.75	1.69 (0.5:2.5)	25.86
	Mo^{6+}	232.36	235.73	2.14 (0.5:2.5)	30.14
Pt_1Ru_2/MoC	Mo^{2+}	228.57	231.72	0.83 (0.5:2.5)	35.88
	Mo^{4+}	229.16	232.49	1.74 (0.5:2.5)	34.00
	Mo^{6+}	232.12	235.47	2.50 (0.5:2.5)	30.12

Table S5. Summary of binding energy shifts used to decouple alloying and support effects.

Comparison	Purpose	Pt $4f_{7/2}$ BE (eV)	Pt Δ BE (eV)	Ru $3p_{3/2}$ BE (eV)	Ru Δ BE (eV)
Pt/C→ Pt_1Ru_2/C	Alloy effect on Pt (Pt-Ru coordination on same support)	71.9→ 72.3	+0.4	-	-
Ru/C→ Pt_1Ru_2/C	Alloy effect on Ru (Pt-Ru coordination on same support)	-	-	461.2→ 460.6	-0.6
Pt_1Ru_2/C→ Pt_1Ru_2/MoC	Support effect on alloy (same composition, different supports)	72.3→ 72.1	-0.2	461.2→ 461.6	+1.0
Pt/C→ Pt/MoC	Support effect on Pt (single metal)	71.9→ 72.0	+0.1	-	-
Ru/C→ Ru/MoC	Support effect on Ru (single metal)	-	-	461.2→ 461.4	+0.2

Note: The alloy effect is extracted by comparing samples on the same carbon support: i) Pt/C vs Pt_1Ru_2/C and Ru/C vs Pt_1Ru_2/C. The Pt $4f_{7/2}$ peak shifts from 71.9 eV (Pt/C) to 72.3 eV (Pt_1Ru_2/C), corresponding to ΔBE = +0.4 eV, while the Ru $3p_{3/2}$ peak shifts from 461.2 eV (Ru/C) to 460.6 eV (Pt_1Ru_2/C) (ΔBE = −0.6 eV). These comparisons isolate the electronic modulation arising from Pt-Ru coordination without involving the MoC support. Meanwhile, to identify the support effect, we follow the reviewer's recommendation and directly compare the same alloy composition on different supports: Pt_1Ru_2/C vs Pt_1Ru_2/MoC. Upon switching the support from carbon to MoC, the Pt $4f_{7/2}$ peak changes from 72.3 eV to 72.1 eV (ΔBE = −0.2 eV), and the Ru $3p_{3/2}$ peak changes from 460.6 eV to 461.6 eV (ΔBE = +1.0 eV). These additional shifts, observed at fixed alloy stoichiometry, demonstrate that MoC introduces an extra and quantifiable electronic modulation beyond the alloying effect. For completeness, we also compared Pt/C vs Pt/MoC (ΔBE (Pt $4f_{7/2}$) = +0.1 eV) and Ru/C vs Ru/MoC (ΔBE (Ru $3p_{3/2}$) = +0.2 eV), further confirming that MoC can electronically perturb both Pt and Ru sites.

Table S6. Summary of the HOR performances for different catalysts.

Sample	Loading (μg_{PGM} cm^{-2})	$j_{0,m}$ (A mg_{PGM}^{-1})	$j_{k,m}$ (MA) (A mg_{PGM}^{-1})	ECSA-10ug (m^2 g_{PGM}^{-1})	$j_{0,s}$ (mA cm^{-2})
Pt/MoC		0.32	1.34	59.21	1.08
Pt/C_{com}		0.13	0.35	55.14	0.47
Pt/C		0.09	0.21	32.45	0.55
Ru/MoC		0.27	0.75	45.37	1.20
Ru/C_{com}	5	0.18	0.41	35.43	1.04
Ru/C		0.15	0.26	30.94	0.94
Pt_1Ru_2/MoC		0.62	3.88	99.85	1.24
$PtRu/C_{com}$		0.40	2.89	81.58	0.98
Pt_1Ru_2/C		0.23	0.71	69.58	0.67

Table S7. Summary of the reported alkaline HOR performances for different catalysts.

Catalyst	Loading ($\mu g_{PGM}\ cm^{-2}$)	$j_{0,\ m}$ ($A\ mg_{PGM}^{-1}$)	$j_{k,\ m}$ ($A\ mg_{PGM}^{-1}$)	Ref.
Pt/MoC		**0.32**	**1.34**	
Ru/MoC	**5**	**0.27**	**0.75**	**This work**
Pt_1Ru_2/MoC		**0.62**	**3.88**	
PtRu/Mo_2C-TaC	13	0.15	0.41	[4]
$PtRu_3$/PC	16	0.33	2.81	[5]
PtRu NWs	20	0.02	0.60	[6]
$Ru_{0.90}Pt_{0.10}$/C	6.98	0.21	0.24	[7]
$Ru_{0.2}Pt_{0.8}$	7.09	0.20	0.41	[8]
$(Pt_{0.9}Pd_{0.1})_3Fe$	5	0.31	0.99	[9]
Pd_3Co@Pt/C	6.98	0.04	0.18	[10]
$Co_{0.2}Ru_{0.7}Pt_{0.1}$/PNC NSs	15	0.29	1.84	[11]
HEA PdNiRuIrRh NPs	6.98	0.07	3.25	[12]
O-PdFe@Pt/C	5	0.24	0.25	[13]
PtIr DNWs/C	10.2	0.07	3.48	[14]
PtRh NAA	25	0.34	0.32	[15]
O-Pt_3In/rGO	10	0.30	2.31	[16]
PtMo/MoO_{x-1}/C	9.43	0.41	3.19	[17]

$Ir/\alpha\text{-}MoC_{1-x}$	4.26	0.32	0.32	[18]
$Pt_{SA}Mo_2C$-NC	10	0.27	2.15	[19]
Ir@Pd	20	0.36	1.20	[20]
PdCu/C-500°C	12.5	0.13	0.52	[21]
Ru_1Ir_1/C	33.6	0.35	1.42	[22]
$Ru_{0.8}Pd_{0.2}/C$	7.04	0.12	0.18	[23]
$IrWO_x/C$	2.01	0.67	2.16	[24]
Ru SA/WC_{1-x}	37.29	0.11	0.88	[25]
Mo-Ru-2/C	6	0.54	1.86	[26]
Ru/RuO_2	20	0.44	1.20	[27]
Ru_3Sn_7/C	7.05	0.29	0.66	[28]
Ru-Ru_2P/C	8.33	0.38	1.27	[29]
Ru/MnO	20	0.19	0.78	[30]
IO-Ru-TiO_2/C	25.48	0.02	0.91	[31]
Rh_2Sb NBs/C*	12.75	0.46	3.25	[32]
Mo-Pt/NC	10	1.18	4.55	[33]
PtPd@PdCu HNPs/W-CNTs	15	0.67	3.48	[34]
Pt_6 NCs/C	5	0.65	3.66	[35]
Pt SACs/CrN	4.5	1.11	2.84	[36]

Table S8. Summary of the reported cost-normalized HOR performance for different catalysts.

Catalyst	Loading (μg_{PGM} cm^{-2})	j_0^{cost} (A USD^{-1})	j_k^{cost} @50 mV (A USD^{-1})	Ref.
Pt/MoC		**3.36**	**14.05**	
Ru/MoC	**5**	**5.47**	**15.19**	**This work**
Pt_1Ru_2/MoC		**8.57**	**53.61**	
PtRu/Mo_2C-TaC	13	2.07	5.66	[4]
$PtRu_3$/PC	16	5.42	46.16	[5]
PtRu NWs	20	0.28	8.29	[6]
$Ru_{0.90}Pt_{0.10}$/C	6.98	3.89	4.45	[7]
$Ru_{0.2}Pt_{0.8}$	7.09	2.32	4.76	[8]
$(Pt_{0.9}Pd_{0.1})_3Fe$	5	3.34	10.67	[9]
Pd_3Co@Pt/C	6.98	0.52	2.36	[10]
$Co_{0.2}Ru_{0.7}Pt_{0.1}$/PNC NSs	15	5.26	33.38	[11]
HEA PdNiRuIrRh NPs	6.98	0.50	23.17	[12]
O-PdFe@Pt/C	5	2.91	3.03	[13]
PtIr DNWs/C	10.2	0.45	22.60	[14]
PtRh NAA	25	1.48	1.40	[15]
O-Pt_3In/rGO	10	4.18	32.20	[16]

$PtMo/MoO_{x-1}/C$	9.43	4.30	33.45	[17]
$Ir/\alpha\text{-}MoC_{1-x}$	4.26	1.46	1.46	[18]
$Pt_{SA}Mo_2C\text{-}NC$	10	2.83	22.54	[19]
Ir@Pd	20	2.50	8.32	[20]
PdCu/C-500°C	12.5	1.86	7.45	[21]
Ru_1Ir_1/C	33.6	2.61	10.59	[22]
$Ru_{0.8}Pd_{0.2}/C$	7.04	2.24	3.37	[23]
$IrWO_x/C$	2.01	3.06	9.88	[24]
Ru SA/WC_{1-x}	37.29	2.23	17.82	[25]
Mo-Ru-2/C	6	10.94	37.67	[26]
Ru/RuO_2	20	8.91	24.30	[27]
Ru_3Sn_7/C	7.05	5.91	13.46	[28]
$Ru\text{-}Ru_2P/C$	8.33	7.70	25.72	[29]
Ru/MnO	20	3.85	15.80	[30]
IO-Ru-TiO_2/C	25.48	0.41	18.43	[31]
Rh_2Sb NBs/C*	12.75	1.27	8.95	[32]
Mo-Pt/NC	10	12.37	47.70	[33]
PtPd@PdCu HNPs/W-CNTs	15	8.11	42.13	[34]
Pt_6 NCs/C	5	6.81	38.37	[35]

Pt SACs/CrN	4.5	11.64	29.78	[36]

Note: The metal prices of Pt, Ru, Pd, Rh, Ir and Ni are 95.38 USD g^{-1}, 49.38 USD g^{-1}, 69.84 USD g^{-1}, 363.32 USD g^{-1}, 218.69 USD g^{-1} and 0.01 USD g^{-1}, respectively.

$$\text{Cost-normalized } j \text{ (A USD}^{-1}) = \frac{j}{PGM\ Price_{\ aera}}$$

where: j is the area-normalized current density, including the exchange current density j_0 or the kinetic current density j_k@50 mV (A cm^{-2}), PGM $Price_{aera}$ is the noble-metal cost per unit electrode area (USD cm^{-2}), calculated as:

$$PGM\ Price_{aera} = \sum_i^n L_i \times P_i$$

where: L_i is the loading of noble metal on the electrode (g cm^{-2}); P_i is the market price of noble metal (USD g^{-1}); i refers to Pt, Ru, or other metals present in the catalyst.

Table S9. Pt 4f XPS spectra fitting parameters of Pt_1Ru_2/MoC before and after the ADT.

Catalyst	Pt species	$4f_{7/2}$ BE (eV)	$4f_{5/2}$ BE (eV)	FHWM (eV)	Proportion (%)
Pt_1Ru_2/MoC	Pt^0	72.09	75.55	1.64 (0.5:3.5)	75.10
Initial	$Pt^{\delta+}$	74.46	77.73	2.50 (0.5:3.5)	24.90
Pt_1Ru_2/MoC	Pt^0	72.14	75.58	1.73 (0.5:3.5)	73.78
after the ADT	$Pt^{\delta+}$	74.51	77.71	2.50 (0.5:3.5)	26.22

Table S10. Ru 3p XPS spectra fitting parameters of Pt_1Ru_2/MoC before and after the ADT.

Catalyst	Ru species	$3p_{3/2}$ BE (eV)	$3p_{1/2}$ BE (eV)	FHWM (eV)	Proportion (%)
Pt_1Ru_2/MoC	Ru^0	462.96	484.60	3.5 (0.5:3.5)	64.23
Initial	$Ru^{\delta+}$	469.68	492.54	3.5 (0.5:3.5)	35.77
Pt_1Ru_2/MoC	Ru^0	462.95	484.63	3.5 (0.5:3.5)	64.24
after the ADT	$Ru^{\delta+}$	469.66	492.51	3.5 (0.5:3.5)	35.76

Table S11. Mo 3d XPS spectra fitting parameters of Pt_1Ru_2/MoC before and after the ADT.

Catalyst	Mo species	$3d_{5/2}$ BE (eV)	$3d_{3/2}$ BE (eV)	FHWM (eV)	Proportion (%)
Pt_1Ru_2/MoC Initial	Mo^{2+}	228.67	231.89	0.85 (0.5:2.5)	34.73
	Mo^{4+}	229.42	232.70	1.90 (0.5:2.5)	31.30
	Mo^{6+}	232.36	235.63	2.50 (0.5:2.5)	33.97
Pt_1Ru_2/MoC after the ADT	Mo^{2+}	228.67	231.87	0.84 (0.5:2.5)	32.34
	Mo^{4+}	229.43	232.71	1.94 (0.5:2.5)	32.81
	Mo^{6+}	232.37	235.67	2.50 (0.5:2.5)	34.85

Table S12. Pt 4f XPS spectra fitting parameters of Pt_1Ru_2/C before and after the ADT.

Catalyst	Pt species	$4f_{7/2}$ BE (eV)	$4f_{5/2}$ BE (eV)	FHWM (eV)	Proportion (%)
Pt_1Ru_2/C	Pt^0	72.03	75.57	1.34 (0.5:3.5)	53.71
Initial	$Pt^{\delta+}$	73.27	76.92	2.23 (0.5:3.5)	46.29
Pt_1Ru_2/C	Pt^0	72.19	75.68	1.35 (0.5:3.5)	41.19
after the ADT	$Pt^{\delta+}$	73.65	77.15	2.50 (0.5:3.5)	58.81

Table S13. Ru 3p XPS spectra fitting parameters of Pt_1Ru_2/C before and after the ADT.

Catalyst	Ru species	$3p_{3/2}$ BE (eV)	$3p_{1/2}$ BE (eV)	FHWM (eV)	Proportion (%)
Pt_1Ru_2/C	Ru^0	463.18	485.55	3.5 (0.5:3.5)	73.39
Initial	$Ru^{\delta+}$	468.70	490.75	3.5 (0.5:3.5)	26.61
Pt_1Ru_2/C	Ru^0	463.78	485.77	3.5 (0.5:3.5)	54.09
after the ADT	$Ru^{\delta+}$	469.26	491.01	3.5 (0.5:3.5)	45.91

Table S14. Calculated Gibbs free energy changes along the alkaline HOR reaction pathway on different catalysts.

Catalyst	Clean surface* (eV)	*→*H (eV)	*H→*H+*OH (eV)	*H+*OH→*+H_2O (eV)
Pt/C	0	-0.69	-0.27	0.96
Pt/MoC	0	-0.46	-0.14	0.60
Ru/C	0	-0.51	-0.71	1.22
Ru/MoC	0	-0.51	-0.24	0.75
Pt_1Ru_2/C	0	-0.47	-0.27	0.74
Pt_1Ru_1/MoC	0	-0.15	-0.28	0.43
Pt_1Ru_2/MoC	0	-0.38	-0.09	0.47
Pt_1Ru_3/MoC	0	-0.21	-0.46	0.67
Pt_1Ru_4/MoC	0	-0.57	-0.12	0.69

Note: The Gibbs free energy of the clean surface was defined as the reference state. ($\Delta G = 0$ eV).

References

1. M. Ernzerhof and G. E. Scuseria, *The Journal of Chemical Physics*, 1999, **110**, 5029-5036.
2. J. Hafner, *Journal of Computational Chemistry*, 2008, **29**, 2044-2078.
3. J. Zhang, T. Wang, P. Liu, Z. Liao, S. Liu, X. Zhuang, M. Chen, E. Zschech and X. Feng, *Nature Communications*, 2017, **8**, 15437.
4. E. R. Hamo, R. K. Singh, J. C. Douglin, S. Chen, M. B. Hassine, E. Carbo-Argibay, S. Lu, H. Wang, P. J. Ferreira, B. A. Rosen and D. R. Dekel, *ACS Catalysis*, 2021, **11**, 932-947.
5. J. Zhang, X. Qu, L. Shen, G. Li, T. Zhang, J. Zheng, L. Ji, W. Yan, Y. Han, X. Cheng, Y. Jiang and S. Sun, *Small*, 2021, **17**, 2006698.
6. M. E. Scofield, Y. Zhou, S. Yue, L. Wang, D. Su, X. Tong, M. B. Vukmirovic, R. R. Adzic and S. S. Wong, *ACS Catalysis*, 2016, **6**, 3895-3908.
7. S. St. John, R. W. Atkinson III, K. A. Unocic, R. R. Unocic, T. A. Zawodzinski Jr and A. B. Papandrew, *ACS Catalysis*, 2015, **5**, 7015-7023.
8. S. St. John, R. W. Atkinson, III, R. R. Unocic, T. A. Zawodzinski, Jr. and A. B. Papandrew, *The Journal of Physical Chemistry C*, 2015, **119**, 13481-13487.
9. T. Zhao, G. Wang, M. Gong, D. Xiao, Y. Chen, T. Shen, Y. Lu, J. Zhang, H. Xin, Q. Li and D. Wang, *ACS Catalysis*, 2020, **10**, 15207-15216.
10. T. Zhao, Y. Hu, M. Gong, R. Lin, S. Deng, Y. Lu, X. Liu, Y. Chen, T. Shen, Y. Hu, L. Han, H. Xin, S. Chen and D. Wang, *Nano Energy*, 2020, **74**, 104877.
11. Z. Qiu, Y. Li, Y. Gao, Z. Meng, Y. Sun, Y. Bai, N. T. Suen, H. C. Chen, Y. Pi and H. Pang, *Angewandte Chemie International Edition*, 2023, **62**, e202306881.

12. Y. Men, D. Wu, Y. Hu, L. Li, P. Li, S. Jia, J. Wang, G. Cheng, S. Chen and W. Luo, *Angewandte Chemie International Edition*, 2023, **62**, e202217976.

13. W. Xiao, W. Lei, J. Wang, G. Gao, T. Zhao, M. A. L. Cordeiro, R. Lin, M. Gong, X. Guo, E. Stavitski, H. L. Xin, Y. Zhu and D. Wang, *Journal of Materials Chemistry A*, 2018, **6**, 11346-11352.

14. M. Wang, M. Wang, C. Zhan, H. Geng, Y. Li, X. Huang and L. Bu, *Journal of Materials Chemistry A*, 2022, **10**, 18972-18977.

15. Y. Jin, F. Chen, J. Wang, L. Guo, T. Jin and H. Liu, *Journal of Power Sources*, 2019, **435**, 226798.

16. J. Wu, X. Gao, G. Liu, X. Qiu, Q. Xia, X. Wang, W. Zhu, T. He, Y. Zhou, K. Feng, J. Wang, H. Huang, Y. Liu, M. Shao, Z. Kang and X. Zhang, *Journal of the American Chemical Society*, 2024, **146**, 20323-20332.

17. H. Luo, K. Wang, F. Lin, F. Lv, J. Zhou, W. Zhang, D. Wang, W. Zhang, Q. Zhang, L. Gu, M. Luo and S. Guo, *Advanced Materials*, 2023, **35**, 2211854.

18. Y. Han, L. Zhao, W. Cheng, M. Wang, L. Yang, Y. Lin and K. Xu, *Advanced Functional Materials*, 2024, **34**, 2407060.

19. X. Yang, W. Yu, Y. Zhang, C. Qiao, L. Liu, Y. Zhang, Q. Li, M. Mou, R. Wang, X. Yuan, Z. Wang, L. Yan and X. Zhao, *Journal of Colloid and Interface Science*, 2025, **692**, 137489.

20. B. Zhang, G. Zhao, B. Zhang, L. Xia, Y. Jiang, T. Ma, M. Gao, W. Sun and H. Pan, *Advanced Materials*, 2021, **33**, 2105400.

21. Y. Qiu, L. Xin, Y. Li, I. T. McCrum, F. Guo, T. Ma, Y. Ren, Q. Liu, L. Zhou, S. Gu, M. J. Janik and W. Li, *Journal of the American Chemical Society*, 2018, **140**, 16580-16588.

22. B. Qin, H. Yu, X. Gao, D. Yao, X. Sun, W. Song, B. Yi and Z. Shao, *Journal of Materials Chemistry*

A, 2018, **6**, 20374-20382.

23. S. St. John, R. W. Atkinson III, R. R. Unocic, T. A. Zawodzinski Jr and A. B. Papandrew, *The Journal of Physical Chemistry C*, 2015, **119**, 13481-13487.

24. L. Fu, F. Yang, Y. Hu, Y. Li, S. Chen and W. Luo, *Science Bulletin*, 2020, **65**, 1735-1742.

25. J. Park, H. Kim, S. Kim, S. Y. Yi, H. Min, D. Choi, S. Lee, J. Kim and J. Lee, *Advanced Materials*, 2023, **36**, 2308899.

26. Y. Zhao, D. Wu and W. Luo, *ACS Sustainable Chemistry & Engineering*, 2022, **10**, 1616-1623.

27. X. Zhang, L. Xia, G. Zhao, B. Zhang, Y. Chen, J. Chen, M. Gao, Y. Jiang, Y. Liu, H. Pan and W. Sun, *Advanced Materials*, 2023, **35**, 2208821.

28. L. Su, X. Fan, Y. Jin, H. Cong and W. Luo, *Small*, 2023, **19**, 2207603.

29. Y. Jin, X. Fan, W. Cheng, Y. Zhou, L. Xiao and W. Luo, *Angewandte Chemie International Edition*, 2024, **63**, e202406888.

30. S. Zhang, R. Ren, J. Cao, D. Zhang, J. Bai, C. Han, L. Xiao, L. Zhuang, P. Song and W. Xu, *Advanced Energy Materials*, 2025, **15**, 2404266.

31. J. Jiang, S. Tao, Q. He, J. Wang, Y. Zhou, Z. Xie, W. Ding and Z. Wei, *Journal of Materials Chemistry A*, 2020, **8**, 10168-10174.

32. Y. Zhang, G. Li, Z. Zhao, L. Han, Y. Feng, S. Liu, B. Xu, H. Liao, G. Lu and H. L. Xin, *Advanced Materials*, 2021, **33**, 2105049.

33. M. Ma, G. Li, W. Yan, Z. Wu, Z. Zheng, X. Zhang, Q. Wang, G. Du, D. Liu, Z. Xie, Q. Kuang and L. Zheng, *Advanced Energy Materials*, 2022, **12**, 2103336.

34. R. Yan, J. Li, L. Zhao, D. Liu, Y. Long, B. Mao, D. Wang, Y. Dai and C. Hu, *Nano Letters*, 2024,

24, 4849-4857.

35. X. Wang, L. Zhao, X. Li, Y. Liu, Y. Wang, Q. Yao, J. Xie, Q. Xue, Z. Yan and X. Yuan, *Nature Communications*, 2022, **13**, 1596.

36. Z. Yang, C. Chen, Y. Zhao, Q. Wang, J. Zhao, G. I. N. Waterhouse, Y. Qin, L. Shang and T. Zhang, *Advanced Materials*, 2023, **35**, 2208799.